Combustion Instability in Solid Rocket Motors: Final Report

Ben Couchman and Kelly Mathesius

December 2017

Abstract

Since the development on the V-2 in the 1930s, combustion instability has been a significant concern for all rocket engine development programs. Combustion instability is generally characterized as oscillations in the combustion process, which can (and often do) couple to other aspects of the rocket motor such as the fluid dynamics or the structural modes. Due to the large energy fluxes present in rocket engines, if even a small fraction of the energy enters mechanical modes, it can result in destruction of the rocket engine. Clearly the prediction of combustion instability is an important part of rocket engine design. However due to the complexity of the processes involved, many simplifying assumptions are used to make the problem tractable.

We assess five of these simplified combustion response models by comparison to experimental data. All the models relied on user supplied coefficients. While, these coefficients had some relation to physical parameters of the combustion process, it was no sufficient to be able to obtain reasonable *a priori* predictions. We derived a model for combustion stability based on the quasi-one dimensional steady (QSHOD) model, and the burn rate model of Lengelle et al for ammonium-perchlorate/binder propellants. The purpose was to obtain a combustion response model that was a function of design level propellant parameters (such as ammonium perchlorate loading and particle diameter) that the user can specify, and 'universal' coefficients for the propellant (such as binder decomposition Arrhenius coefficients) which the user would not need to modify. Unfortunately, the newly derived model performed poorly in comparison to experimental data and so is not fit for predictive capabilities.

At the lowest pressure the best performing model allowed for the effect of a process with a time lag that is constant with respect to forcing frequency. This model predicted an additional peak (compared to the other models) at a frequency inline with that predicted by Boggs layer frequency concept, which is physically consistent with a constant time-lag approximation. We hypothesis that the combustion pressure is sufficiently low that there is no longer a molten layer of ammonium perchlorate at the propellant surface. Under these conditions, layers of ammonium perchlorate particles are exposed as the propellant regresses, which results in this low frequency peak in the response function. Due to the lack of low frequency data, it is difficult to confirm this hypothesis.

At all pressures the ZN model outperforms the QSHOD model. The ZN model includes the effect of pressure sensitivity on the surface pyrolysis reaction, which the QSHOD model does not. Thus, the pressure sensitivity for that surface pyrolysis reaction is important and cannot be neglected in the surface response prediction.

The ZNR model outperforms the ZN model, particularly at higher pressures. The ZNR model includes the effect of radiative heating of virgin propellant by the combustion gases. As the combustion pressure increases, the combustion temperature increases. Radiative heat-flux scales as T^4, thus as the pressure increases the effect of radiative heat transfer can no longer be neglected.

The ZNR model was coupled to a first order (linearized) acoustics model and compared to experimental data for a full motor configuration. We used the acoustics model to predict the pressure responses of a full-scale motor configuration, with comparisons made against the data of Blomshield et al. While this model was not able to determine if the system was stable or unstable, it was able to recover the correct trend in pressure decay rate with propellant web.

1 Introduction

Solid rocket motors consist of a mixture of fuel, oxidizer, and other additives that is cast and cured into a solid [1]. Solid propellants can typically be classified broadly in one of the following categories [1]:

1. Double-base propellants consist of a **homogeneous** propellant grain utilizing highly-energetic components containing both fuel and oxidizer. Double-base solid rocket motors typically contain a mixture of nitrocellulose and nitroglycerin, along with several other additives.

2. Composite propellants consist of a **heterogenous** propellant grain utilizing fuel, oxidizer, and other additives bound in a polymer matrix. A typical composite propellant might include ammonium perchlorate as the oxidizer, aluminum powder the as fuel, and hydroxyl terminated polybutadiene as the polymer binder.

The propellant is cured and stored in the combustion chamber itself, and all exposed surfaces of the propellant burn after ignition. The mass flow rate of exhaust gas produced from the burning propellant surface is found using:

$$\dot{m} = A_b r \rho_b \tag{1}$$

where A_b is the propellant burn area, r is the propellant burn rate, and ρ_b is the propellant density. The propellant burn rate (per unit area) r is typically determined using the following empirical equation:

$$r = ap^n \tag{2}$$

where p is the combustion chamber pressure, a is the burn rate coefficient, and n is the burn rate exponent. The values for a and n are experimentally determined, and for a given propellant, the burn rate exponent n must have a value less than one or else the motor pressure will be unstable with respect to burning area and steady-state burning cannot be achieved.

1.1 Steady-State Combustion Mechanism

To discuss the stability of solid rocket motor combustion, it is first necessary to understand the combustion process. We note that the combustion process is not fully understood and this is, in part, responsible for the difficulty in prediction and modelling of combustion instability.

The combustion mechanisms for double-base and composite propellants differ considerably, so both will be reviewed in the next two sections.

1.1.1 Combustion Mechanisms of Double-Base Propellants

Combustion of double-base propellants can be described in the following five zones, starting below the propellant surface and moving spatially through the flame [2]:

1. Preheated propellant zone: The solid propellant is preheated by heat conduction from the surface, but no chemical changes occur.

2. Degraded solid propellant zone: The propellant decomposes to yield nitrogen dioxide and aldehydes. The nitrogen dioxide oxidizes the aldehydes at the burning surface such that the energy balance of this step is exothermic.

3. Primary combustion zone: This is the first step in the gas-phase reaction zone. A reaction including nitrogen dioxide, aldehydes, and small amounts of other species such as hydrogen, carbon, and oxygen occurs, forming nitric oxide, carbon monoxide, water, hydrogen, and carbon-containing species.

4. Dark zone: Nitric oxide, carbon monoxide, hydrogen, and carbon-containing species undergo a series of oxidation reactions, yielding nitrogen, carbon dioxide, water, and other species. However, heat release in this region is too low for a luminous flame to be present.

[1] Some propellants combine properties of both categories, but these formulations are not in common use

5. Secondary combustion zone: Assuming the pressure is high enough, greater than approximately 1 MPa, the final combustion products are formed and thermal equilibrium is achieved in the secondary combustion zone, or flame zone. A flame zone will not be present if the pressure is too low. In this scenario, the reduction of nitric oxide occurs too slowly for nitrogen to form and a flame to be produced.

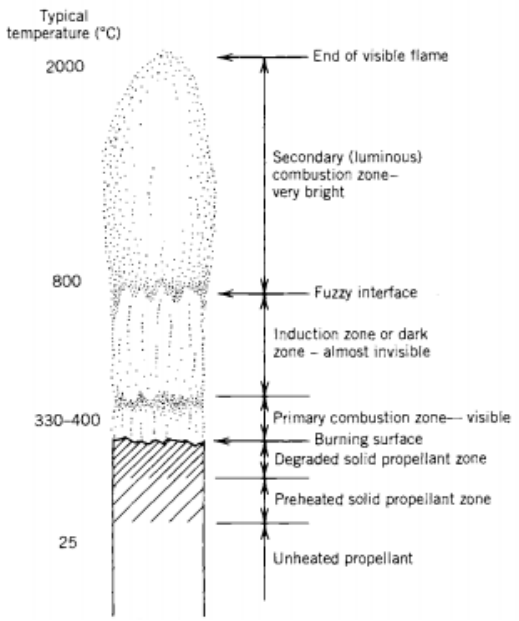

Figure 1: Combustion Zones for a Burning Double-Base Propellant [1]

1.1.2 Combustion Mechanisms of Composite Propellants

The combustion of composite propellants can be described in the following three zones [3]:

1. Preheated propellant zone: The solid propellant is preheated by conduction from the surface, but no chemical changes occur.

2. Degraded solid propellant zone: Oxidizer crystals in the heterogeneous propellant mixture degrade into smaller fragments and the binder decomposes into hydrocarbons and hydrogen. In the case of an Ammonium Perchlorate/Hydroxyl Terminated Polybutadiene (AP/HTPB) composite propellant, the AP oxidizer degrades into perchloric acid, as well as nitrogen- and oxygen-containing species that become oxidizers in the combusion zone reactions. The HTPB binder degrades through depolymerization into hydrocarbon fragments, including ethelyne and other light species.

3. Combustion zone: The decomposition products of the oxidizer, binder, and fuel emerge unmixed into the combustion zone, given that the propellant is a heterogeneous mixture. Therefore, a driving factor in reactions in the combustion zone is the diffusion of these products. These products undergo multi-staged reactions to produce the final combustion products and achieve thermal equilibrium. In the case of an AP/HTPB composite propellant, fragments of perchloric acid, ethylene and other light hydrocarbons, and melted metal fuel react to form water, carbon dioxide, hydrochloric acid, metal oxide, and other trace species.

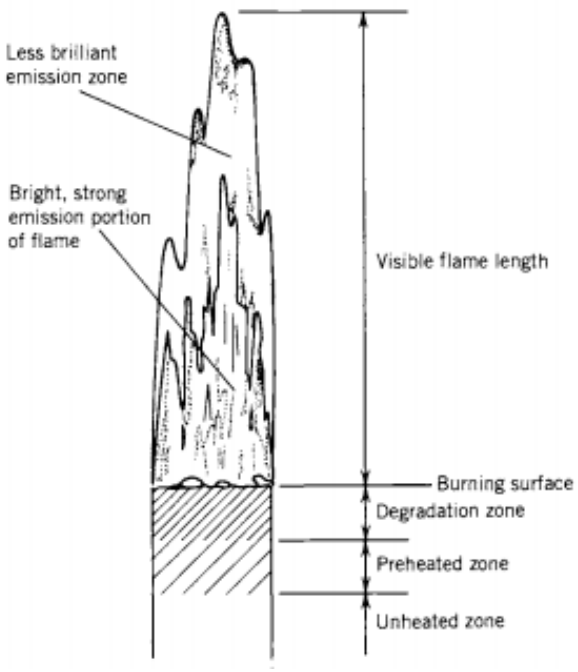

Figure 2: Combustion Zones for a Burning Composite Propellant [1]

2 Mechanisms and Phenomenology

2.1 Acoustic Energy Balance and Combustion Instability

A powerful interpretation of the solid rocket motor is that it can be considered as comprising of two coupled processes: the combustion process, and the acoustic process (see Fig. 3). These processes are coupled by

1. The response of the combustion process to the acoustic disturbance. That is, the change in combustion rate to a pressure disturbance.

2. The response of the solid rocket motor acoustics to a disturbance in combustion rate. That is, the change in the fluid dynamic properties (pressure and velocity) to a disturbance in the propellant burn rate.

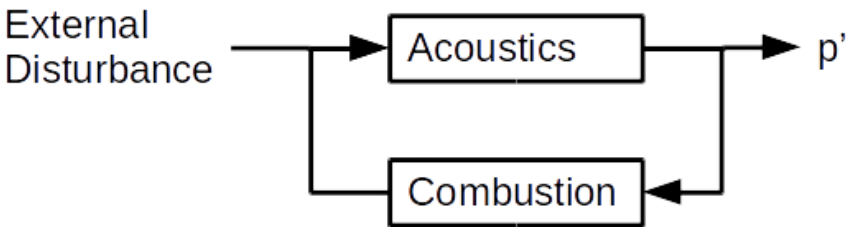

Figure 3: Solid Rocket Motor as a Feedback System

The stability (or instability) of solid rocket motor combustion is due to a balance between phenomena which generate acoustic energy, and those which absorb acoustic energy. Acoustic energy can be generated by the following processes [1]:

1. Fluctuations in the velocity of gasses leaving combustion zone.

2. Pressure and burn rate coupling in combustion zone.

3. Interactions between flow oscillations in the combustion zone and the main flow.

4. Vortex shedding and impingement.

Acoustic energy can be dissipated by the following mechanisms:

1. Energy in longitudinal modes leave the system through the nozzle in the exhaust.

2. Visco-elasticity of the propellant, particularly at elevated temperatures.

3. The boundary layer present over the propellant and the walls damps acoustic energy due to viscous dissipation.

4. Particles and droplets dissipate acoustic energy if they are in a volume of oscillating gas. The drag on the particle / droplet acts to dissipate acoustic energy in the same way that a viscous boundary layer does.

Note that the last item - particle damping - is a commonly used method to stabilize solid motor combustion. Low smoke (i.e. unmetalized) APCP propellants often include a small amount (order of 1%) of refactory particles, such as aluminum oxide or zirconium carbide. This is specifically to utilize the dissipation of acoustic energy around particles. Due to the nonlinearity of their mechanism, it is very difficult for linear stability theory to capture their effect correctly

Combustion within a solid rocket motor will be stable if acoustic energy gains are not larger than acoustic energy losses [4]. If conservation of energy is considered, then in order for the combustion of a solid rocket motor to be stable, the following inequality must be true:

$$\frac{\partial E}{\partial t} + \nabla \cdot W = D < 0 \tag{3}$$

where E represents the system energy, W represents the work done on the system, and D represents total summation of all sources and sinks of energy in the flow.

The thermoacoustic nature of this instability can be demonstrated using the Rayleigh criterion, which determines if changes in acoustic energy in a flow will amplify or suppress flow oscillations [5]. The Rayleigh parameter is defined as the time averaged product of pressure and heat release (q) during one period of flow oscillation, denoted as $\overline{p'q'}$. Using the Rayleigh criterion, if the following inequality is satisfied, then the global combustion mechanism is liable to have instabilities:

$$\int_V \overline{p'q'} dV > 0 \tag{4}$$

2.2 Instability Mechanisms

There are broadly three types of combustion instability: (1) instabilities due to surface combustion; (2) instabilities due to residual combustion in the main volume of the motor; and (3) instabilities due to vortex shedding within the solid rocket motor.

2.2.1 Surface Combustion Instabilities

The combustion process of a solid rocket motor occurs primarily within a thin layer close to the surface of the propellant. Since this is near-universal, regardless of motor size or composition, the surface combustion instabilities are the most widely analyzed.

As outlined in Section 1, the burn rate of solid propellants is dependent on the chamber pressure, and therefore fluctuations in pressure affect the burn rate, and vice versa. Other experiments and theory have also shown a dependence between chamber temperature and burn rate as well [6]. These dependencies mean that variations in these quantities near the burning surface can create oscillations that lead to combustion instabilities.

Culick [6] notes that a part of the chemical energy released during the combustion processes of the propellants transforms into mechanical motion of the exhaust gasses, which can stimulate a feedback path

at the burning surface. Both the propellant burning surface and the combustion chamber itself possess resonant properties. When the resonating frequencies of these two coupled systems are close, conditions for combustion instabilities are present.

The series of steps required to initiate surface combustion instabilities was broadly outlined by Culick [6] as follows:

1. A perturbation such as small change in pressure, temperature, or local gas mixing in the combustion zone causes an increase in reaction rate in the combustion zone.
2. Temperature and energy release in the combustion zone increase due to the increased reaction rate.
3. The amount of heat transferred to the burning surface from the combustion zone increases, causing an increase in temperature and gas production rate at the burning surface.
4. Heat flow into the subsurface region of the propellant increases due to the increased temperature at the burning surface.
5. Subsurface decomposition reaction rates will tend to increase because of the increased heat flow to the region.
6. Temperature will further increase in the subsurface region as exothermic reactions occur, which subsequently increases the gas production rate at the burning surface.
7. If this fluctuation in mass flow leaving the burning surface is in phase with the original perturbation, then the mass production rate at the burning surface is destabilized, and could lead to larger scale surface combustion instabilities.

Culick [6] also describes a more quantitative response function for pressure fluctuations as the dimensionless variable R_p:

$$R_p = \frac{\dot{m}'}{\bar{\dot{m}}} \left[\frac{p'}{p}\right]^{-1} \tag{5}$$

where $\dot{m}$ represents the mass flow due to propellant burning, p represents the chamber pressure, $(*)'$ represents a fluctuation, and $\bar{(*)}$ represents a mean value. He continues by describing the sinusoidal tendencies of the oscillations of mass flow and pressure with the following equations:

$$\frac{\dot{m}'}{\bar{\dot{m}}} = \frac{\hat{\dot{m}}}{\bar{\dot{m}}} e^{i\omega t} \tag{6}$$

$$\frac{p'}{p} = \frac{\hat{p}}{p} e^{i\omega t} \tag{7}$$

where $\hat{(*)}$ represents the amplitude of an oscillation. Rearranging, Culick shows that an oscillation in mass flow can be found in terms of a pressure oscillation and the response function:

$$\frac{\hat{\dot{m}}}{\bar{\dot{m}}} = R_p \frac{\hat{p}}{p} \tag{8}$$

Thus R_p is the transfer function of pressure disturbance to burn-rate disturbance. Being a complex value, it contains both gain and phase information on the resulting perturbations.

Blomshield [7] notes that in an APCP motor, the particle size has a significant impact on the combustion stability. If the particles are too small ($< 5\mu m$) then the pressure coupled response will be significant. However, if the particles are too large ($> 200\mu m$), then stability problems can also occur, coupled with increased non-linear acoustic erosivity. Higher burning rates (all else being equal) result in a lower pressure coupled response as do low burn rate pressure exponents.

While the pressure coupled response is a strong function of pressure, it is not monotonic. That is there will be some pressure at which the response function is largest, and deviations to lower or higher pressures will result in a reduction in its value.

2.2.2 Residual Volume Combustion Instabilities

Typically combustion of the propellant is restricted to a thin region near the surface of the grain. However, in propellants with high metal loading, small droplets of metal may pass through the primary combustion zone near the propellant surface and undergo combustion in the main volume of the motor. Whether this mechanism is a source of instability is still a matter of debate. As a whole this mechanism is particularly poorly understood.

Gallier and Godfroy [5] modeled the effects of aluminum combustion in the main volume of the chamber and argued that it drove combustion instabilities. They detail that resulting combustion instabilities are thermoacoustic and caused by the coupling of chamber acoustics and aluminum combustion mechanisms. In another study, Gallier et al. [8] detail that fluctuations in the mass release rate of aluminum combustion are influenced primarily by fluctuations in axial gas velocity . When an aluminum droplet leaves the burning surface of the propellant, it is expected that it will disturb the flame as it moves with an axial velocity component through the flame. This convective disturbance causes the flame area and heat release to fluctuate, and potentially incites combustion instabilities.

This instability mechanism may also result from a reduction in alumina particles in the volume of the combustion chamber to damp acoustic energy, as the combustion process is still producing them.

2.2.3 Vortex Shedding Instabilities

For larger solid rocket motors, the propellant consists of several grains which have been separately cast [9]. These segmented motors have slots and cavities present between each grain, where propellant combustion is also present. The injection of combustion products into the main volume of the motor causes vortices to form near the propellant surface surrounding the slot. Examples of the vortex structures are given in Fig. 4.

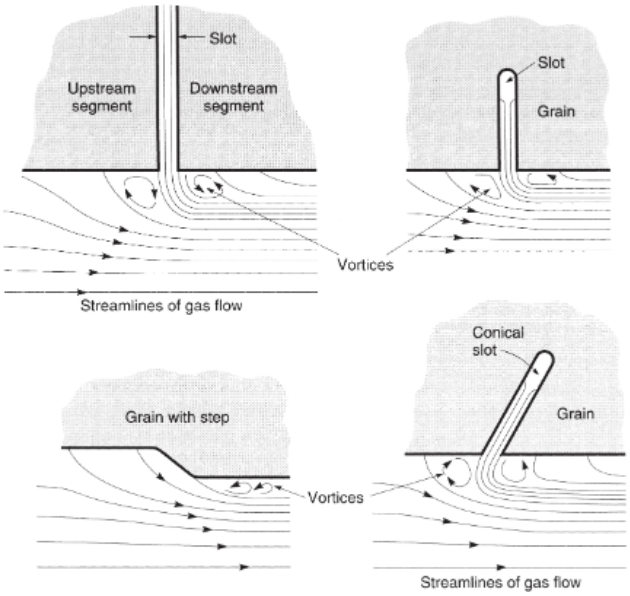

Figure 4: Vortex Shedding Mechanisms [1]

Instabilities caused by vortex shedding typically maintain a low frequency, with pressures oscillating by less than 0.5% [9]. Although not typically destructive to motor function, in poorly designed motors, the shedding of these vortices causes unstable flow in the motor. Furthermore, the shedding of these vortices can couple to existing acoustic instabilities, compounding the instability.

This instability is typically only present in motors which are sufficiently large that the propellant must be cast as separate grains, rather than a single monolithic grain. However, unstable boundary layers at the burning surface of the propellant can also cause vortices to be shed [4]. In addition to vortex shedding, periodic vortex impingement on a hard surface, such as the combustion chamber wall, can also cause pressure fluctuations. If the frequencies of any of these vortex shedding phenomena are close to the resonant

frequency of the combustion chamber, then the coupling of these mechanisms could lead to larger combustion instabilities.

2.3 Manifestation of Combustion Instabilities

Regardless of the combustion instability mechanism, combustion instabilities typically manifest themselves as periodic oscillating pressure waves in the combustion chamber of the motor [10]. Combustion instabilities produce a mean pressure shift, or DC pressure shift, in the chamber, which can be catastrophic in a poorly designed motor. When analyzing the pressure waves in the frequency domain, spectral peaks are visible. These peaks correspond to the longitudinal modes of the combustion chamber, and are related to the coupling between the combustion instabilities and the resonant properties of the combustion chamber. Pressure plots illustrating these phenomena can be seen in Fig. 5.

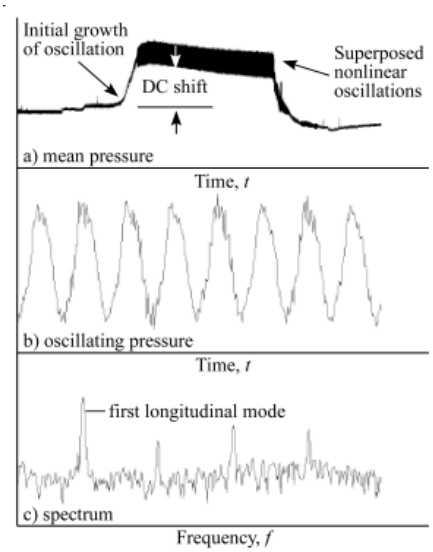

Figure 5: Representative Pressure Measurements for Unstable Combustion [10]

Additionally, after combustion instabilities are initiated, the system limits sufficiently large pressure oscillations due to non-linearities and settle into a limit cycle [6]. Parameters of the specific solid rocket motor, such as combustion chamber geometry and propellant composition, characterize the amplitude and period of the limit cycle.

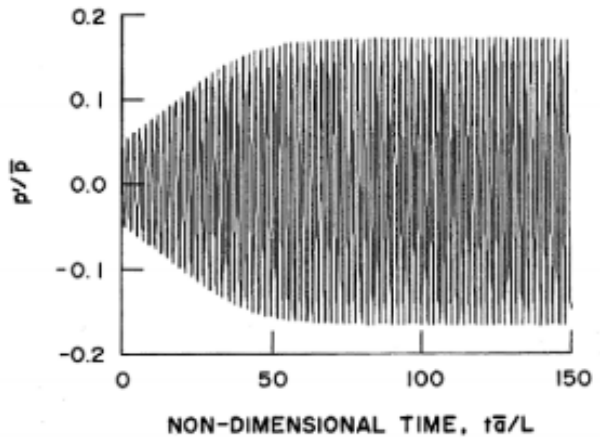

Figure 6: Numerical Simulation of Pressure Oscillation in a Solid Rocket Motor Reaching a Limit Cycle [6]

As is shown in Fig. 6, sufficiently large, unsteady pressure oscillations due to combustion instabilities grow in amplitude until a stable limit cycle is reached. At this point, small perturbations in the pressure oscillations will simply develop back into the limit cycle.

3 Combustion Response Models

Our focus is on the combustion instability aspect of the problem. For this reason, we will be considering a range of combustion stability models, focusing on the surface combustion instabilities.

3.1 The Quasi-Steady Homogeneous One Dimensional (QSHOD) Model

Following the insight of Hart and McClure [11], that the characteristic heat conduction time in the solid is an order of magnitude (or more) greater than the gas phase transport and kinetic timescales, leads to a series of models (starting with the model of Hart and McClure) based on the assertion that the gas-phase is in equilibrium at all times during combustion instability. That is the time-lag in the solid phase which is the dominating physical process.

Over the following decade many models based on this underlying physical process were derived [11, 12, 13, 14, 15]. We refer to these as as the QSHOD model (following Culick). The QSHOD model is named from the assumptions that underlie it:

1. quasi-steady except for unsteady heat transfer in the solid phase
2. homogeneous material properties that are constant with temperature and pressure
3. one-dimensional models
4. Instantaneous solid to gas phase transition

We refer to these models as a single model because, as shown by Culick [16], these models result in identical dynamics. That is,

$$\frac{\dot{m}'}{\bar{\dot{m}}}\left[\frac{p'}{p}\right]^{-1} = \frac{nAB}{\lambda + (A/\lambda) - (1+A) + AB}, \tag{9}$$

where A and B are non-dimensional parameters defined by

$$A = \left(1 - \frac{T_i}{T_s}\right)\frac{T_a}{T_s}, \tag{10}$$

$$B = \frac{\frac{T_i}{T_s}}{j(1 - \frac{T_i}{T_s})}, \tag{11}$$

where j is the index in the initial-temperature-dependent burn rate law $\dot{m} \sim p^n {T_i}^j$. Furthermore, λ is obtained by solving

$$\lambda\left(\lambda - 1\right) = i\Omega, \tag{12}$$

for the root with the positive real term, and Ω is the non-dimensional frequency $\Omega = \frac{\kappa_p \rho_B \omega}{\dot{m}^2 c}$, c is the specific heat capacity of the propellant, and κ_p is the thermal conductivity of the propellant. Some (minor) variation in the result exists between different authors due to differences in the assumptions used for modelling the gas phase.

Using the result above, Culick [16] was then able to show a linear stability estimate,

$$\left(B + 1\right) \geq A\left(B - 1\right), \tag{13}$$

which reflects the fact that the stability of combustion is a function of the solid phase thermal response and the gas phase.

The QSHOD model splits the solid motor combustion process into three regions:

1. Solid phase
2. Solid-gas interface
3. Gas phase

These regions are shown schematically in Fig. 7

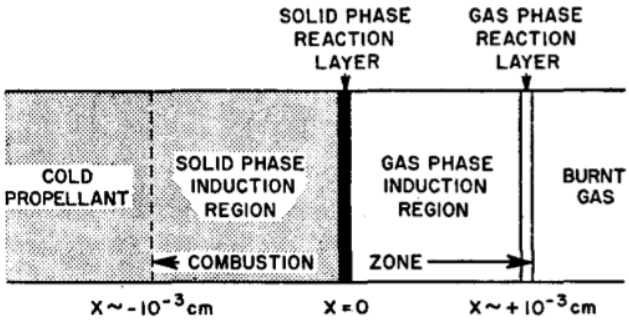

Figure 7: Combustion Process Used by QSHOD Model [13]

The solid phase, referring to the unburnt propellant, is treated as a 1D, homogeneous material with constant properties. Rather than a pyrolysis zone, the transition from solid to gas is assumed to occur instantaneously. The solid-gas interface is governed by conservation of mass and energy, as well as a model for the solid-gas conversion process. Typically an Arrhenius law is assumed. However, since the model is linearized about a single point, the exact form of this term is not important. Modelling of the gas phase is the most complicated, and is treated slightly differently by the various authors. For example, Denison and Baum [15] assume equal diffusion coefficients for all species and species diffusion due to concentration gradient only, where as Hart et al [14] do not include any diffusion effects. Since the gas phase is assumed to equilibrate instantaneously, the effect of the simplifications has little effect on the final result. This coupled set of models is linearized about the steady state solution and a perturbation analysis is performed.

3.2 Zel'dovich - Novozhilov (ZN) Model

In 1942, Zel'dovich [17], using the same assumption that the solid phase thermal transients are the dominant low frequency effect (but almost 20 years before Hart and McClure) developed a theoretical framework for the combustion and explosion of solid materials. Novozhilov extended this work to the stability of solid rocket motors [18, 19]. The resulting model can be thought of as almost equivalent to the QSHOD model, but including the effect of pressure on the surface pyrolysis rate. The model requires definitoin of four parameters:

$$k = (T_s - T_i)\left(\frac{\partial \log \dot{m}}{\partial T_i}\right)_p, \tag{14}$$

$$r = \left(\frac{\partial T_s}{\partial T_i}\right)_p, \tag{15}$$

$$\nu = \left(\frac{\partial \log \dot{m}}{\partial \log p}\right)_{T_i}, \tag{16}$$

$$\mu = \frac{1}{T_s - T_i}\left(\frac{\partial T_s}{\partial \log p}\right)_{T_i}. \tag{17}$$

Using these parameters, the response function is derived as,

$$\frac{\dot{m}'}{\bar{\dot{m}}}\left[\frac{p'}{p}\right]^{-1} = \frac{\nu + (\nu r - \mu k)(\lambda - 1)}{r(\lambda - 1) + k\left(\frac{1}{\lambda}\right) + 1}. \tag{18}$$

Comparing the definitions in this section to those used in the QSHOD model, we see that,

$$A = \frac{k}{r}, \tag{19}$$

$$B = \frac{1}{k}, \tag{20}$$

$$n = \nu. \tag{21}$$

After making these substitutions, we can see that this result is nearly equivalent to the QSHOD model. This is unsurprising since the assumptions made during the construction of the Zel'dovich - Novozhilov model are the same as those of the QSHOD model. However, using the combustion analysis of Zel'dovich resulted in dependence on a different (although related) set of physical parameters, which are easier to obtain from experiment. Novozhilov went on to obtain explicit (linear) stability criteria, either (1) $k < 1$, or (2) $r > (k-1)^2/k + 1$.

The flexibility of the Zel'dovich - Novozhilov model has allowed it to be used in a several linear stability estimates for response to non-sinusoidal disturbances [20, 21].

3.3 ZN Model with Condensed Phase Radiative Heating Corrections (ZNR)

Brewster and Son [22], and Zebrowski and Brewster [23] examine the validity of assuming that the solid phase reaction is a zeroth-order Arrhenius type reaction located at the propellant surface. By introducing a slightly more complex model for the burn rate from Ibiricu and Williams [24], they were able to derive new forms for the Zel'dovich parameters to account for radiative heating of the propellant, which can be significant,

$$r = \frac{k\left[2 - Q_c - Q_r\right] - 1}{\left(1 - \frac{T_i}{T_s}\right)(1+E)\left(2 - Q_c - 2Q_r\right) - 1}, \tag{22}$$

$$\mu = \frac{\nu\left[2 - Q_c - Q_r\right]}{\left(1 - \frac{T_i}{T_s}\right)(1+E)\left(2 - Q_c - 2Q_r\right) - 1}, \tag{23}$$

$$\delta = \frac{-\nu}{\left(1 - \frac{T_i}{T_s}\right)(1+E)\left(2 - Q_c - 2Q_r\right) - 1}. \tag{24}$$

The Q_c and Q_r are non-dimensional heating values, defined as,

$$Q_c = \frac{L_s}{c_p\left(T_s - T_i\right)}, \tag{25}$$

$$Q_r = f_r J, \tag{26}$$

where L_s is the condensed-phase heat release (note positive is exothermic), f_r is the fraction of incident radiative heat-flux absorbed below the surface reaction zone, and J is a non-dimensionalized form of the radiative heat-flux (q),

$$J = \frac{q}{c_p\left(T_s - T_i\right)} \tag{27}$$

With these parameters defined, they define the following response function:

$$\frac{\dot{m}'}{\bar{\dot{m}}}\left[\frac{p'}{p}\right]^{-1} = \frac{nAB + n_s\left(\lambda - 1\right)}{\lambda + \left(A/\lambda\right) - \left(1 + A\right) + AB - \frac{Q_r A(\lambda-1)}{\beta+\lambda-1}}, \tag{28}$$

We need to define the optical thickness of the conduction zone (β), as

$$\beta = \frac{\alpha_c}{r}\frac{5 f_v}{k}, \tag{29}$$

where α_c is the thermal diffusivity of the propellant, f_v is the carbon loading volume fraction, and k is the characteristic wavelength (taken as $1.5\mu m$ from [22]). We assume the radiative heat-flux incident to the

surface is black-body radiation from the combustion gases. That is $q = \epsilon\sigma T^4$, where we use $\epsilon = 0.33$ from calculations by Brewster and Son [22].

They also introduce new parameters to account for radiative heat transfer (q) to the reaction zone from the gas phase, however we do not have suitable data available to assess it

$$\nu_q = \left(\frac{\partial \log \dot{m}}{\partial \log q}\right)_{T_i,p}, \tag{30}$$

$$\mu_q = \frac{\nu_q \left[2 - Q_c - Q_r\right] - Q_r}{\left(1 - \frac{T_i}{T_s}\right)(1+E)(2 - Q_c - 2Q_r) - 1}, \tag{31}$$

$$\delta_q = \frac{-\nu_q + kQ_r}{\left(1 - \frac{T_i}{T_s}\right)(1+E)(2 - Q_c - 2Q_r) - 1}. \tag{32}$$

This allows introduction of a new response function,

$$\frac{\dot{m}'}{\bar{\dot{m}}}\left[\frac{q'}{\bar{q}}\right]^{-1} = \frac{\nu_q AB + n_q(\lambda - 1) - \frac{Q_r A(\lambda-1)}{\beta+\lambda-1}}{\lambda + (A/\lambda) - (1+A) + AB - \frac{Q_r A(\lambda-1)}{\beta+\lambda-1}}, \tag{33}$$

which is the frequency response function driven by radiative heating. Based on the nonlinear analysis performed in their work, it is suggested that the transient in the propellant phase transition is more important than the gas phase kinetics. Furthermore, they call in to question the assumption involved in using a zeroth-order, single-step Arrhenius model for the entire solid-to-gas transition process.

3.4 QSHOD Model with Surface Layer Time Lag (QSHOD-τ)

Cheng [25] formulated a modified QSHOD model that accounts for the discrepancy between reaction rates of the combustion processes at the propellant surface versus in the gas phase. He introduced the following response function to account for this difference in reaction rates:

$$\frac{\dot{m}'}{\bar{\dot{m}}}\left[\frac{p'}{p}\right]^{-1} = R_p \frac{e^{-i\Omega\tau}}{\sqrt{1 + (\Omega\tau)^2}}, \tag{34}$$

where R_p is the classic QSHOD response function given in Equation 9, Ω is the dimensionless frequency, and τ is the dimensionless time lag $\tau = T/(\alpha_c/r^2)$, where T is the physical time lag, α_c is the thermal diffusivity of the propellant, and r is the propellant burn rate.

In this model, τ is treated as a constant. However, this introduces a problem where the response function produces oscillatory behavior where the period increases as frequency increases [6]. This is not a realistic combustion response. For most processes that introduce a time-lag, τ is likely a function of Ω. However, if we examine Boggs et al [26] and their analysis of propellant heterogeneousness, there may be an effect that is independent of the driving frequency.

3.5 Shusser-Culick (SC) Model

Shusser and Culick [27] relax the propellant homogeneity assumption to produce a modified QSHOD model that handles oxidizer and binder separately. They consider the response of AP and binder separately before combining the responses as the final step. Separate AP and binder response functions are expressed as follows:

$$R_{AP} = \frac{\dot{m}'_{AP}}{\bar{\dot{m}}_{AP}}\left[\frac{p'}{p}\right]^{-1} \tag{35}$$

$$R_B = \frac{\dot{m}'_B}{\bar{\dot{m}}_B}\left[\frac{p'}{p}\right]^{-1} \tag{36}$$

These response functions are defined using

$$R_{AP} = \frac{n_{AP}B_{AP} + C_{AP}F_B}{[\lambda_{AP}/A_{AP} + 1/\lambda_{AP} - (1 - B_{AP}) - 1/A_{AP}] - (C_{AP}C_B/n_B B_B)F_B}, \tag{37}$$

$$R_B = \frac{n_B B_B + C_B F_{AP}}{[\lambda_B/A_B + 1/\lambda_B - (1 - B_B) - 1/A_B] - (C_{AP}C_B/n_{AP}B_{AP})F_{AP}}. \tag{38}$$

F_{AP} and F_B are the classic QSHOD response functions for AP and binder:

$$F_{AP} = \frac{n_{AP}A_{AP}B_{AP}}{\lambda_{AP} + A_{AP}/\lambda_{AP} - (1 + A_{AP}) + A_{AP}B_{AP}}, \tag{39}$$

$$F_B = \frac{n_B A_B B_B}{\lambda_B + A_B/\lambda_B - (1 + A_B) + A_B B_B}, \tag{40}$$

and C_{AP} and C_B are coupling coefficients. Unlike in the classic QSHOD model, the coefficients in these response functions do not have explicit relationships to physical parameters. A_{AP}, B_{AP}, and n_{AP} can be considered as roughly analogous to the A, B, and n parameters in the classic QSHOD models because AP can self-deflagrate. Conversely, the values for A_b, B_b, and n_b cannot be regarded as analogous as the binder does not burn on its own.

The pressure exponents n_{AP} and n_b are coupled are also related to the propellant burn rate exponent n with the following equations:

$$n_1 = n_{AP} + \frac{C_x}{B_x} n_2 \tag{41}$$

$$n_2 = n_B + \frac{C_f}{B_f} n_1 \tag{42}$$

$$n = \alpha_{AP} n_1 + \alpha_B n_2 \tag{43}$$

The overall response function is found by taking the mass-weighted average of the AP and binder response functions:

$$R_p = \alpha_{AP} R_{AP} + \alpha_B R_B. \tag{44}$$

4 Combustion Stability Results

We compare the models listed in section 3 against data from Blomshield et al [28] for an AP/HTBP propellant with 88% AP loading with $55\mu m$ diameter particles. The data provided is the combustion response determined from T-Burner test at three pressures: 3.45MPa, 6.90MPa, and 10.34MPa.

4.1 QSHOD Model Analysis

A plot of the QSHOD model fit to experimental data at different pressures can be seen in Figure 8 below.

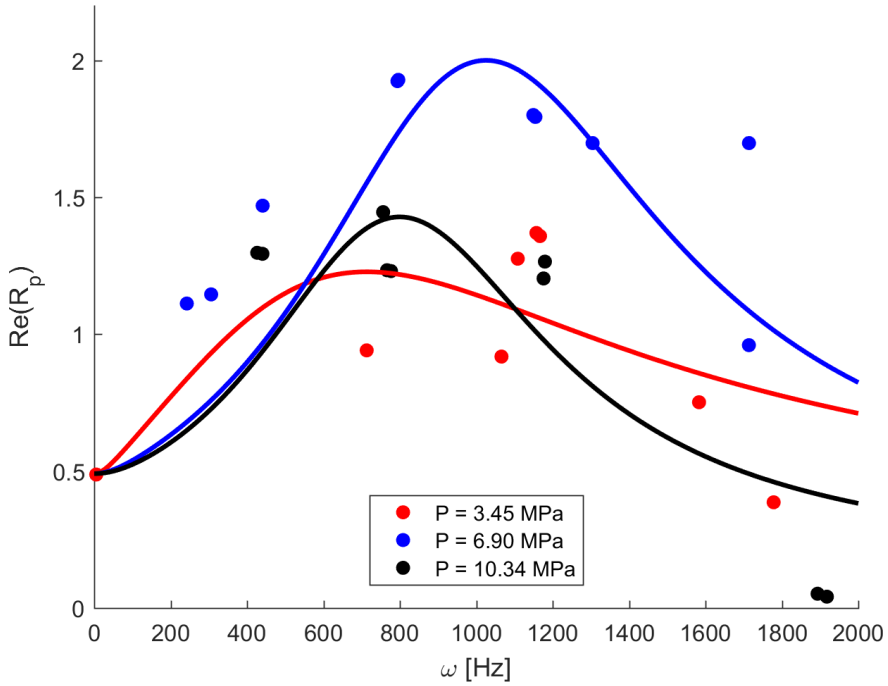

Figure 8: QSHOD Model Fit to Experimental Data [28] at Varying Pressures

Values were fit for parameters A and B in the QSHOD model response function and are given in Table 1. The root mean square error for the fit is also listed.

p [MPa]	A	B	R.M.S Error
3.45	5.773	0.8229	0.2905
6.90	4.322	0.5563	0.2531
10.34	2.773	0.4786	0.3242

Table 1: Model Parameters and R.M.S Errors for QSHOD Model at Varying Pressures

The values for A and B were then used to calculate other relevant but unknown parameter values. The definition of A given in Equation 10 was rearranged to solve for T_a and the definition of B given in Equation 11 was rearranged to solve for j as follows:

$$T_a\left(A\right) = A\frac{1-T_s}{1-\frac{T_i}{T_s}} \tag{45}$$

$$j\left(B\right) = \frac{\frac{T_i}{T_s}}{B\left(1-\frac{T_i}{T_s}\right)} \tag{46}$$

It was assumed that $T_i = 300K$. T_s was taken as mass-weighted average of propellant surface temperatures for AP and binder given by Lengelle et al [29]: $T_s = \alpha_{AP}T_{s,AP} + \alpha_B T_{s,b}$. Using the values in Table 1, the following values for T_a and j at varying pressures are given below.

p [MPa]	$T_a(A)$ [K]	$j(B)$ [-]
3.45	7998	0.5643
6.90	5987	0.8348
10.34	3842	0.9703

Table 2: Model Parameters and R.M.S Errors for QSHOD Model at Varying Pressures

4.2 ZN Model Analysis

The ZN Model was used to fit the data from Lengelle et al [29] and produces a noticeably different curve shape, shown in Figure 9.

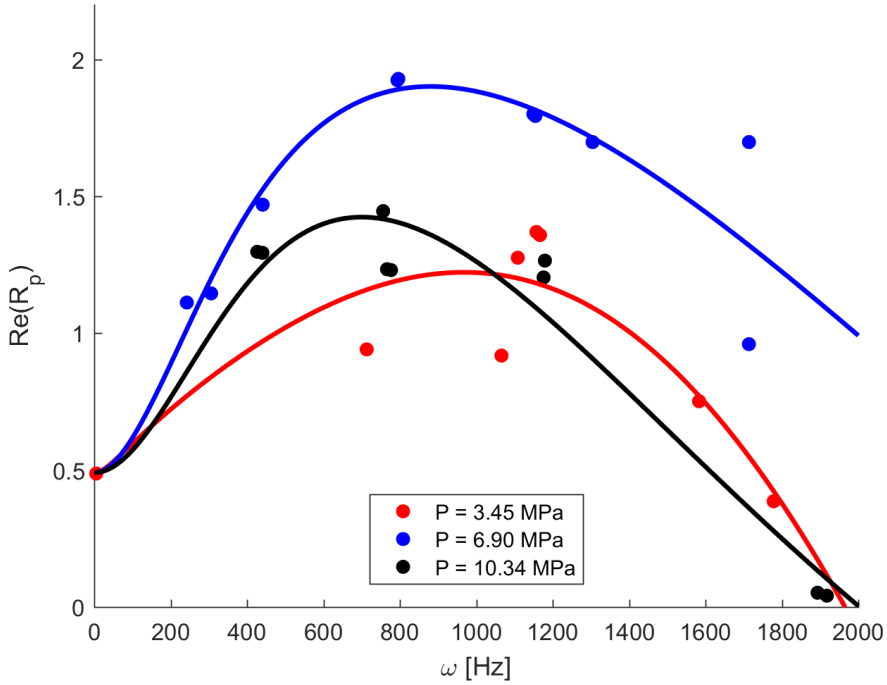

Figure 9: ZN Model Fit to Experimental Data [28] at Varying Pressures

The parameters k, r, and μ from the response function given in Equation 18 were fit to the experimental data, and their fitted values are given in Table 3.

p [MPa]	k	r	μ	R.M.S Error
3.45	1.144	0.0497	0.3896	0.2042
6.90	2.864	0.4444	0.4476	0.0860
10.34	4.068	0.9335	0.4911	0.1489

Table 3: Model Parameters and R.M.S Errors for ZN Model at Varying Pressures

The three parameter values all increase with chamber pressure. When considering the parameter definitions given in Equations 14, 15, and 17. The equivalent A and B parameters, calculated using Eq. 19 and Eq. 20 are given in Table 4 below. In general, the ZN model produces higher A values and lower B values than the QSHOD model. That is, the ZN model suggest that the activation temperature for the propellant combustion reaction is higher than in the QSHOD model does, and also the sensitivity to initial propellant temperature is lower.

p [MPa]	A	B
3.45	23.0	0.974
6.90	6.4	0.349
10.34	4.4	0.9335

Table 4: Effective A and B parametres

4.3 ZNR Model Analysis

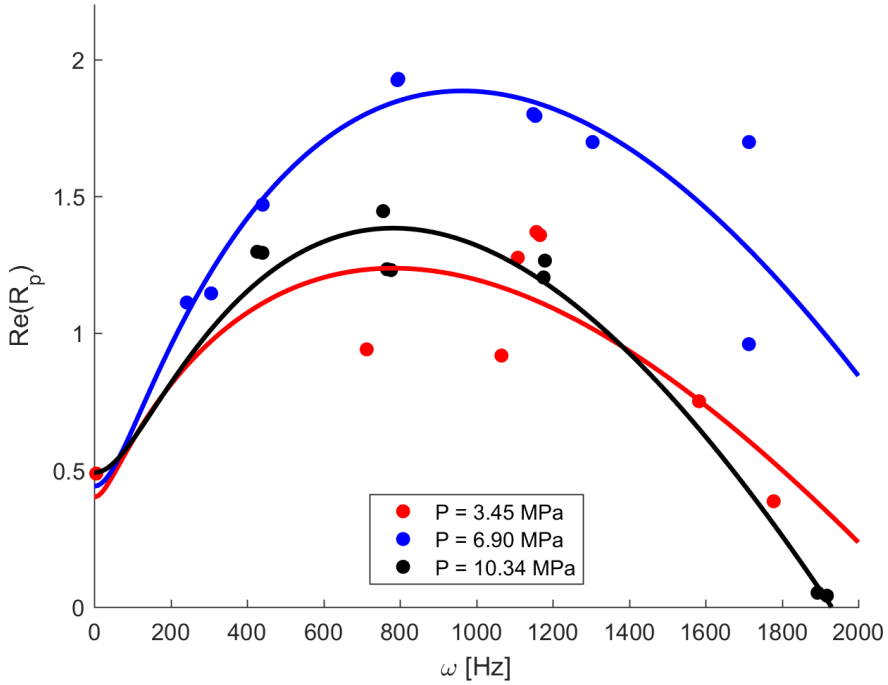

Figure 10: ZNR Model Fit to Experimental Data [28] at Varying Pressures

p [MPa]	k	δ	f_r	R.M.S Error
3.45	0.1085	1.698	0.3520	0.2510
6.90	0.1947	6.988	0.4889	0.0825
10.34	0	4.857	0.4750	0.1041

Table 5: Model Parameters and R.M.S Errors for ZNR Model at Varying Pressures

Its interesting to note that this model predicts much lower values for k, than the ZN model. This is because k is the sensitivity of burn rate to propellant initial temperature; with 35% to 50% of the incident radiative heat being absorbed by the virgin propellant, the effect of the radiative heating dominates the enthalpy associated with the initial propellant temperature.

4.4 QSHOD-τ Model Analysis

The QSHOD-τ Model was implemented with an enforced bound of $\tau > 0$ in the curve fitting. The resulting fitted curves at varying pressures are shown in Figure 11.

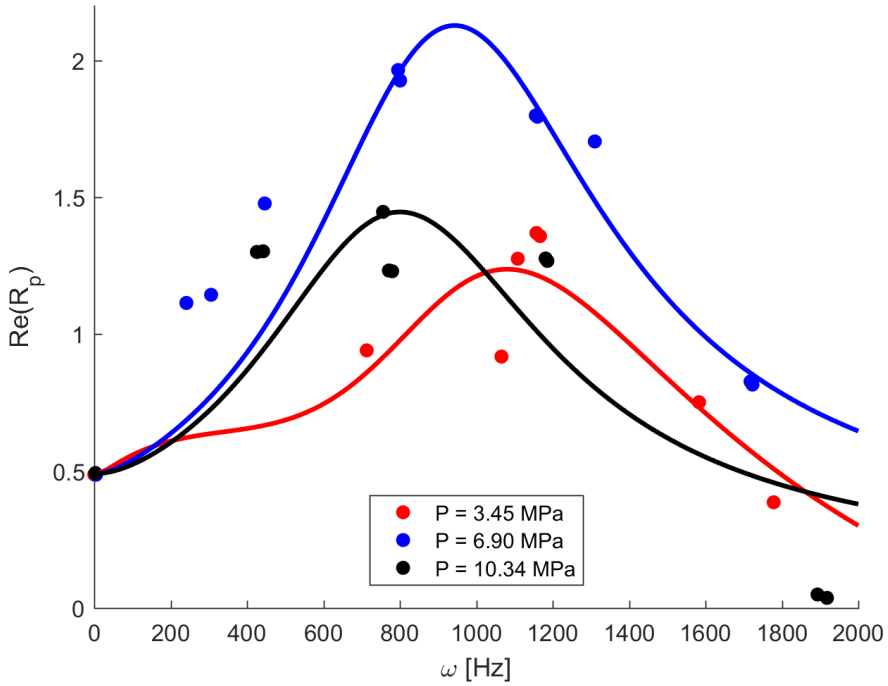

Figure 11: QSHOD-τ Model Fit to Experimental Data [28] at Varying Pressures

The curve fitting procedure set $\tau = 0$ for chamber pressures of 6.90 MPa and 10.34 MPa. The resulting curves for these pressure are therefore identical to the curves for the classic QSHOD Model curves shown in Figure 8.

p [MPa]	A	B	τ	R.M.S Error
3.45	8.097	0.6713	0.1622	0.1845
6.90	4.332	0.5563	0	0.2531
10.34	2.773	0.4787	0	0.3242

Table 6: Model Parameters and R.M.S Errors for QSHOD-τ Model at Varying Pressures

Note that the coefficients are the same as the QSHOD model for the 6.90MPa nad 10.34MPa. However for the 3.45MPa case, a τ of 0.1622 is predicted and results in a 30% lower rms error. This suggests that at lower pressures there may be a process active (which is not active at the higher pressures) with an approximately constant phase lag compared to the input disturbance. For lower pressures (generally around 20atm) the AP is not able to melt, and particles of AP would protrude from the surface of the propellant. Following Boggs et al [26], we calculate that protruding oxidizer particles would excite a mode at approximately 180Hz. We can see that this τ parameter introduces a new peak in the response function at approx. 200Hz. Thus the 3.45MPa propellant may be at sufficiently low pressure not to form an AP melt layer, and there is an excitation due to the solid AP grains protruding the surface at around 200Hz. Note that this mechanism is independent of imposed frequency, meaning the constant time lag model used would be appropriate to model it. We would not expect to see this mode at higher pressures, because the AP particles will form a melt layer and this excitation mode will not exists.

If we perform a similar analysis of the A and B parameters presented in Table 6 as was done for the classic QSHOD parameters in Section 4.1, then we find the following values for $T_a(A)$ and $j(B)$:

p [MPa]	$T_a(A)$ [K]	$j(B)$ [-]
3.45	1122	0.6918
6.90	5987	0.8348
10.34	3842	0.9703

Table 7: Model Parameters and R.M.S Errors for QSHOD Model at Varying Pressures

4.5 SC Model Analysis

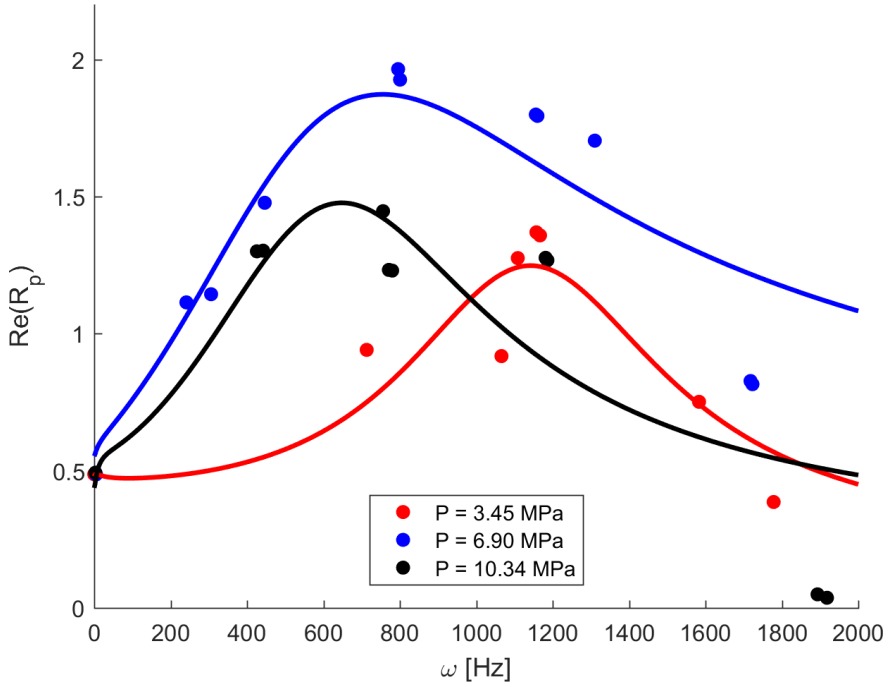

Figure 12: SC Model Fit to Experimental Data [28] at Varying Pressures

The corresponding parameters for the curves are presented for each pressure in Table 8.

p [MPa]	A_B	A_{AP}	B_B	B_{AP}	C_B	C_{AP}	n_{AP}	R.M.S Error
3.45	2.045	11.99	11.88	0.6913	73.27	-0.002893	0.07791	0.4339
6.90	54.35	6.562	11.03	1.233	-0.1117	-2.174	0.5473	0.3358
10.34	7.991	8.297	7.941	2.836	-1.556	-11.47	0.1205	0.4431

Table 8: Model Parameters and R.M.S Errors for SC Model at Varying Pressures

The values for A_{AP} and B_{AP} can be treated somewhat analogously to the A and B parameters used in the classic QSHOD response function model given in Equation 9, and their values are relatively similar to the values given in Table 1.

It it important to not however that the fitted curves in Figure 12 and corresponding parameters in Table 8 are presented tentatively for this model. Given the large number of parameters and relatively few data points, the curve fitting procedure was very sensitive to initial parameter guesses and parameter bounds. Small changes in the initial parameter guesses often led to vastly different output parameters from the curve fitting procedure. Some of these curves are shown in Figure 13 for a chamber pressure of 3.45 MPa.

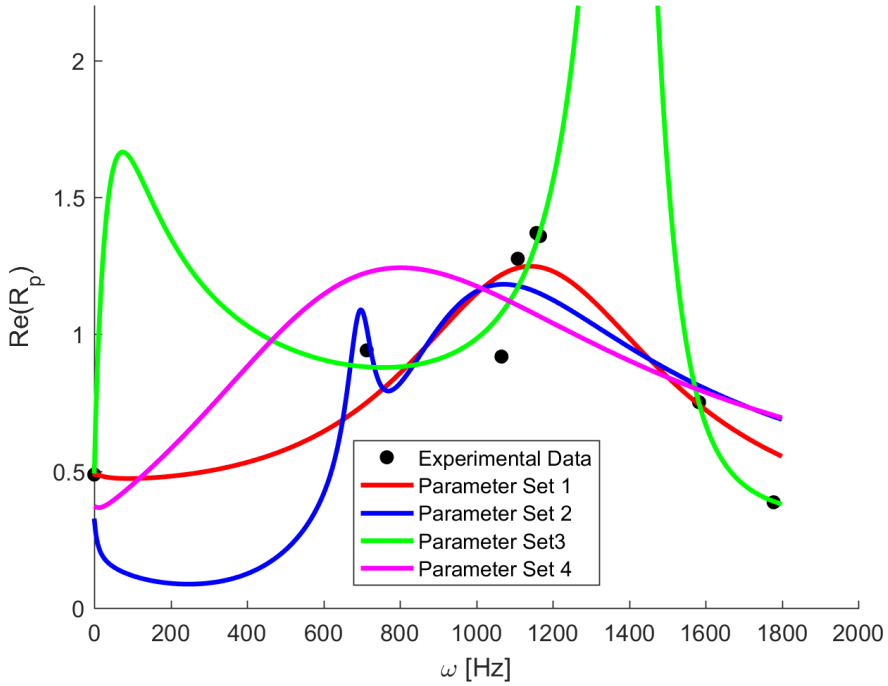

Figure 13: SC Model Curve Fittings at P = 3.45 MPa with Experimental Data [28]

These fitted curves, despite having very different shapes, all have same order R.M.S Errors, which are given in Table 9 along with the corresponding fitted parameters.

Parameter Set	A_B	A_{AP}	B_B	B_{AP}	C_B	C_{AP}	n_{AP}	R.M.S Error
1	2.045	11.99	11.88	0.6913	73.27	-0.002893	0.07791	0.4339
2	52.72	7.785	8.246	0.5567	1.609	-0.03602	0.4857	0.5516
3	29.59	14.37	1.049	0.6694	2.603	-5.231e-06	0.04946	0.2032
4	0.1682	8.303	17.32	0.7498	18.74	-0.8886	0.385	0.6696

Table 9: Parameter Values of Various Curve Fittings for SC Model at P = 3.45 MPa

4.6 Model Comparison

We compare the different models for the 3.45MPa case in Fig. 8 below. Its interesting to note that the best fits to the data are the QSHOD-τ and the SC models. The SC model explicitly includes the effect of heterogeneousness of the propellant and, as hypothesized in section 4.4, the QSHOD-τ model is consistent with excitation due to the AP particles. This suggests that at these lower pressures, the combustion mechanism results in particular sensitivity to the propellant being heterogeneous. The QSHOD-τ correctly returns the steady state limit, while the SC model does not.

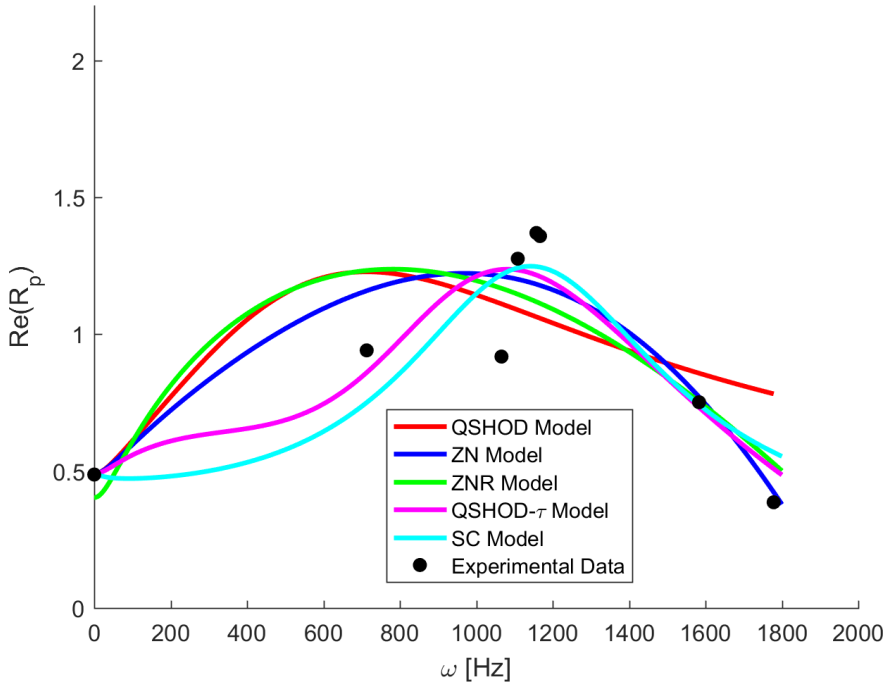

Figure 14: Comparison of Best Fit Curves and Experimental Data [28] for a Chamber Pressure of 3.45 MPa

The predictions for the 6.90MPa case are given in Fig. 15 below. Note that the QSHOD and the QSHOD-τ results are identical, and mostly fail to capture the data except for the general trend. The SC-model performs well in the low frequency regime, suggesting that the effect of hetergeneousness may be important to the low freqency responds. However, the ZN and ZNR models (which do not account for the propellant being heterogeneous) also match well, and do so across all frequencies. This suggests that the dependence of surface pyrolysis to pressure cannot be neglected.

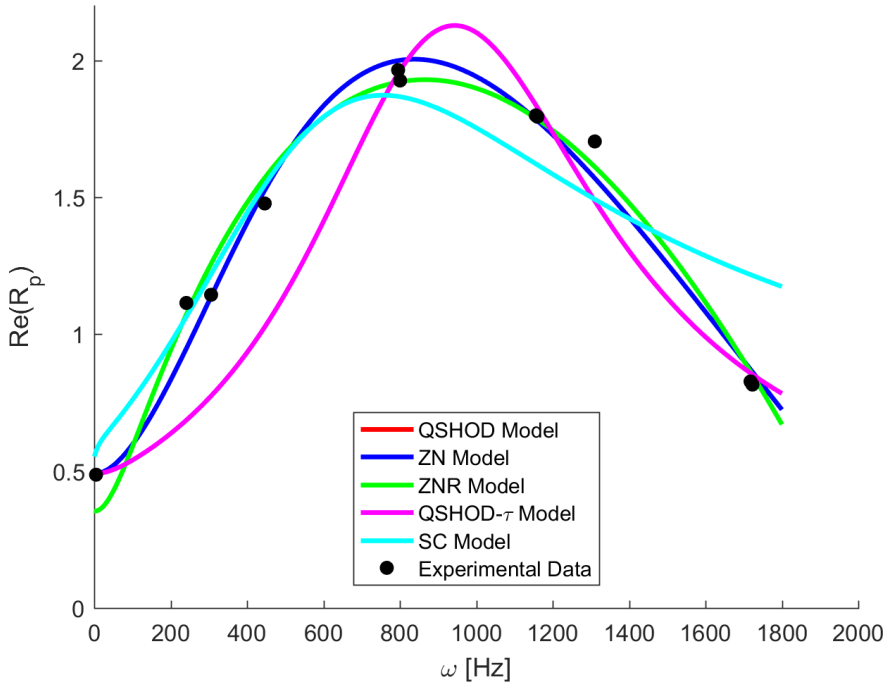

Figure 15: Comparison of Best Fit Curves and Experimental Data [28] for a Chamber Pressure of 6.90 MPa

The results for the different models at 10.34MPa are given in Fig. 16. We can see that the ZNR model performs best out of all the models examined. This suggests that at these higher pressures, the radiative heating to the propellant by the combustion gas is significant. This is reasonable, since increasing combustion pressure also increases combustion temperature, and emitted radiative heat-flux scales as T^4. Thus, at higher pressure,s the preheating of the propellant by radiative heat transfer becomes a significant phenomena.

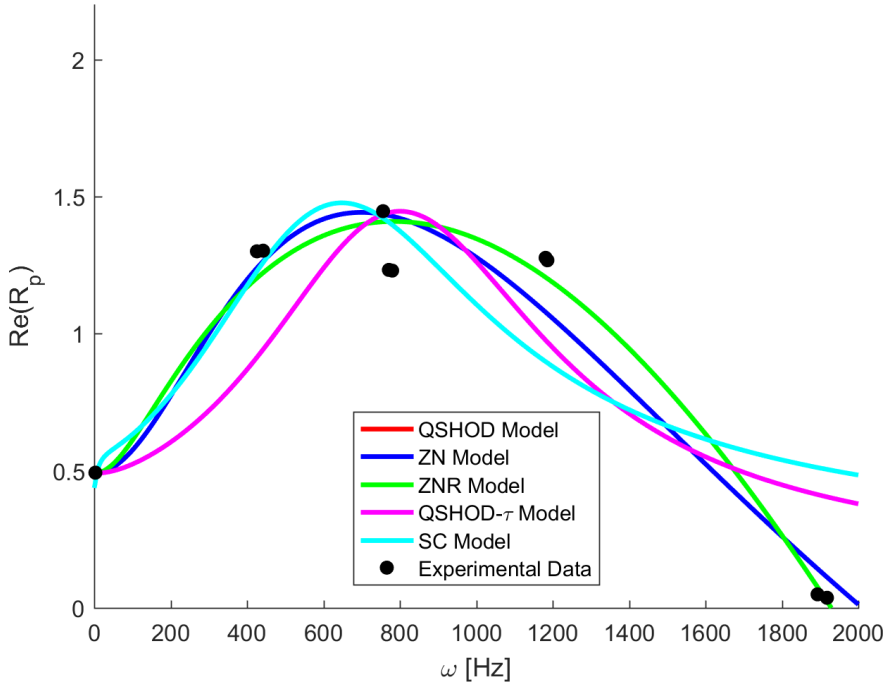

Figure 16: Comparison of Best Fit Curves and Experimental Data [28] for a Chamber Pressure of 10.34 MPa

The root mean square errors of the models for each pressure are given in Table 10, with the best performing model highlighted. For the lowest pressure, the QSHOD-τ model performs the best, where as the ZNR model is the best performing for the other pressures. From this we tentatively hypothesize the following about the combustion process:

1. At low pressures, the combustion dynamics includes a process where the lag is independent of forcing frequency. The low frequency peak predicted by the QSHOD-τ model closely matches the frequency predicted by Boggs frequency layer analysis - where there is a mode associated with the layering of oxidizer in the binder. We suspect that at these lower pressures, the AP surface temperature is too low for form a a molten layer, thus the combustion process 'sees' layers of AP particles as the propellant regresses.

2. At higher pressures, the temperature of the combustion gas is sufficiently high such that the effect of radiative heatflux from the combusted gas preheating the propellant can no longer be neglected.

3. The pressure effect of the surface decomposition rate cannot be neglected when considering combustion response.

Pressure	QSHOD Model	ZN Model	ZNR Model	QSHOD-τ Model	SC Model
3.45 MPa	0.2905	0.2042	0.2510	0.1845	0.4339
6.90 MPa	0.2531	0.0860	0.0825	0.2531	0.3358
10.34 MPa	0.3242	0.1489	0.1041	0.3242	0.4431

Table 10: R.M.S. Errors for All Models at Varying Pressures (Lowest R.M.S. Error Highlighted)

5 New Supply Only Design Parameters (SODP) Model

In the previous section, initial attempts at determining the parameters for the models were made using physical parameters where possible, however it quickly became an exercise to fitting experimental data. If a propellant is sufficiently well characterized, then this is not an issue, however even relatively small changes to the propellant formulation can have significant effects on the response function. For examples Fig. 17 shows the experimental response function for different propellants AP/CTBP, where the only change is the AP particle diameter. We can see that simply changing the oxidizer particle diameter significantly changes the response function. This makes it impractical to use parameters found for one propellant for even a slight variation.

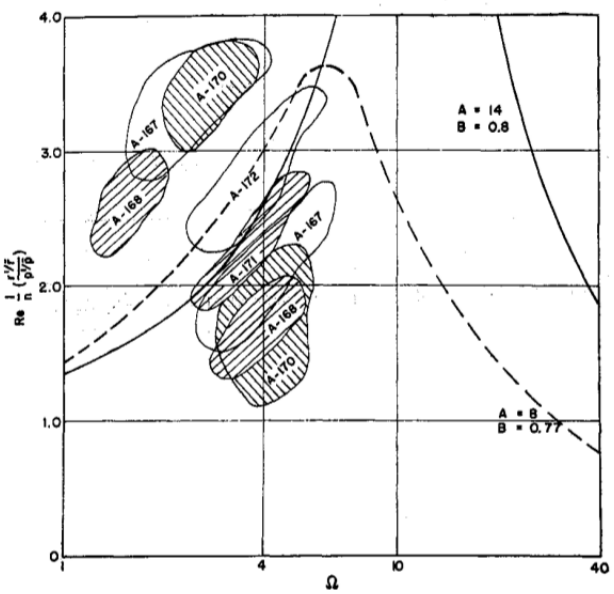

Figure 17: AP/CTPB Results

To that end, we derive our own stability model based on the combustion model of Lengelle et al [29] for AP-binder composite propellants. We do this to derive a model for the response function that does not require fitting to experimental data. That is, a model that depends on design level propellant parameters, which the user can specify, and 'universal' parameters such as the degradation kinetics of AP.

5.1 Combustion Model of Lengelle et al [29]

The combustion model is based on a 'two flame' approximation above semi-infinite columns of AP and binder as shown in Fig. 18. As the AP is heated, it decomposes and sublimates, forming products which burn close to the AP surface (approx. $1\mu m$) and form the lower AP flame. The binder decomposes forming products which burn in a diffusion flame with the AP products. This forms a second (main) flame above the AP flame, which heats the AP flame, and provides the energy to decompose the binder.

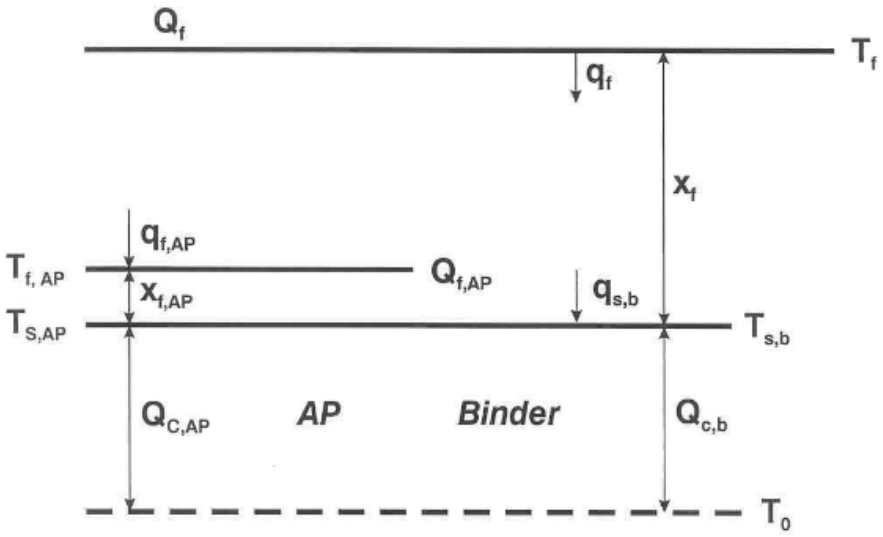

Figure 18: Two-Flame model [30]

We start by considering the combustion of the AP particles in isolation. As the AP is heated, it melts at approximately 835K. This molten AP then proceeds to undergo decomposition and sublimation. Approximately 70% of the AP decomposed primarily forming N_2, N_20, NO, HCl, Cl_2, and O_2. The remaining 30% sublimates into ammonia and perchloric acid. The products, containing both fuel and oxidizer, form a premixed flame approximately $1\mu m$ from the surface of the AP. Since the flame is premixed, the reaction rate is a function of the kinetics, and from experiment the AP reaction rate is given by,

$$w = p^2 A_{g,AP} e^{-\frac{E_{g,AP}}{RT_{f,AP}}} \tag{47}$$

where $A_{g,AP}$ and $E_{g,AP]}$ are given in Appendix A. The burning rate of the AP can also be determined by,

$$m_{AP} = p\sqrt{\frac{\lambda_g A_{g,AP}}{c_{p,g}} e^{-\frac{E_{g,AP}}{RT_{f,AP}} \log\left(1+\frac{c_g\left(T_{f,AP}-T_{s,AP}\right)}{Q_c}\right)}}, \tag{48}$$

where $T_{f,AP}$ and $T_{s,AP}$ are the AP flame and surface temperatures respectively, and Q_c is the energy required to take the AP from molten to gaseous.

We now consider the combustion of the binder. The binder is heated by the main flame, and decomposes, which results in a fuel jet (from the decomposed binder), and an oxidizer jet (from the AP products). Thus, we can see that a diffusion flame will occur in the interface between the binder and AP decomposition products. Thus, in the diffusion limited regime, the flame height can be determined as a function of the AP particle diameter. Furthermore, the effect of the chemical kinetics is included to obtain the following expression for the main flame height,

$$x_f = \dot{m}\left[\frac{c_{p,g}}{8A_d\lambda_g} D_{ox}^2 + \frac{1}{p^2 A_{g,f}} e^{\frac{E_{g,f}}{RT_f}}\right] \tag{49}$$

As well as pyrolyzing the binder, the main flame also supplies heat to the AP flame, increasing its temperature, and so augmenting the rate the AP burns. This additional heating to the AP flame is accounted for using,

$$q_{f,AP} = m_p Q_f e^{-\frac{m_p c_{p,g}\left(x_f - x_{f,A}\right)}{\lambda_g}}, \tag{50}$$

where $x_{f,AP}$ is the height of the AP flame, Q_f is the energy evolved by the main flame, and m_p is the total propellant burning rate.

After restriction to a one dimensional setting, and balancing heat and mass transfer at the surfaces of the AP and the binder, as well as the two flame sheets, the full model is derived. This is a system of non-linear equations that must be solved via the following procedure:

1. Pick a value for $s = \frac{\dot{m}_p}{\dot{m}_{AP}}$
2. Solve the following for the flame temperature of the AP ($T_{f,AP}$)

$$\Delta h_{H,AP} + \Delta h_{D,AP} + c_{p,g}\left(T_{f,AP} - T_{s,AP}\right) = Q_{c,b}\frac{1-\alpha_{AP}}{1-\alpha_{AP}s}\left[1 + \frac{c_{p,g}\left(T_{f,AP} - T_{s,AP}\right)}{Q_c}\right]^s s \tag{51}$$

3. Solve the following for ψ

$$s = \frac{1}{\psi}\sqrt{\frac{e^{\frac{E_{g,AP}}{RT_{f,AP}}}}{A_{g,AP}}\frac{\log\frac{Q_f}{Q_{c,b}}\frac{1-\alpha_{AP}}{1-\alpha_{AP}s}}{\log 1 + \frac{c_{p,g}(T_{f,AP}-T_{s,AP})}{Q_c}}} \tag{52}$$

4. Calculate the combustion pressure (p) from

$$\psi = \frac{c_{p,g}}{8A_d\lambda_g}\left(pD_{ox}\right)^2 + \frac{e^{\frac{E_{g,f}}{RT_f}}}{A_{g,f}} \tag{53}$$

5. Calculate $\dot{m}_{AP}$ from,

$$\dot{m}_{AP} = p\sqrt{\frac{\lambda_g A_{g,AP}}{c_{p,g}}e^{-\frac{E_{g,AP}}{T_{f,AP}}}\log 1 + \frac{c_{p,g}\left(T_{f,AP} - T_{s,AP}\right)}{Q_c}} \tag{54}$$

6. Calculate $\dot{m}_p$ form $\dot{m}_{AP}$ and s

This method has been implemented in matlab and compared to the experimental data provided by Lengelle et al, shown in Fig. 19.

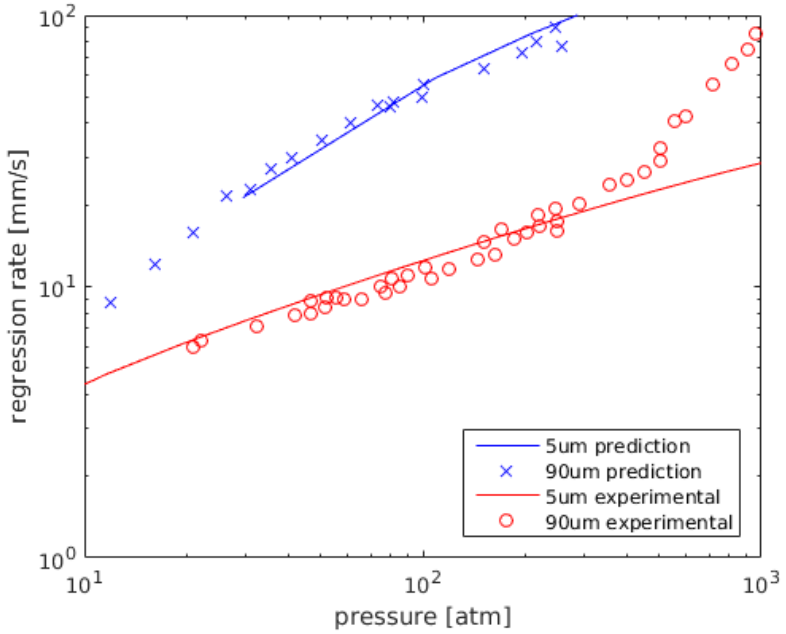

Figure 19: Combustion model of Lengelle et al [29] for 80% AP loading

The values for the coefficients used were fit from experimental data by Lengelle [29] and are listed in appendix A.

5.2 Derivation of Stability Model

Note, in this section, we will use $(*)'$ to be a perturbation and unprimed symbols to be a time averaged quantity. For clarity, we will also drop the $(\dot{*})$ when considering quantities such as mass flow per unit area (m).

In deriving our stability model, we also assume the same 'two flame' approximation above semi-infinite columns of AP and binder. For a semi-infinite material recessing at constant rate, if a sinusoidal temperature perturbation $(\hat{T})$ is applied to the surface with frequency ω, it can be shown that the resulting *perturbed* temperature profile is given by,

$$\frac{T'}{T} = \frac{\hat{T}}{}e^{\lambda \xi_p} e^{-i\omega t}, \tag{55}$$

where $\xi_p = \frac{r}{\alpha_p} x$, and λ is given by the root with positive real part of,

$$\lambda\left(\lambda - 1\right) = -i\frac{\kappa_p \rho_p}{m_p c_p}\omega. \tag{56}$$

We assume that the AP 'column' and the binder 'column' see the same temperature perturbation (i.e. $\hat{T}$ and ω are the same), and the thermal conduction between the two columns are negligible. Under these conditions the spatial frequencies of the AP and binder (λ_{AP} and λ_B respectively) responses are, the positive real-part roots of,

$$\lambda_B\left(\lambda_B - 1\right) = -i\frac{\kappa_B \rho_B}{m_B c_{p,B}}\omega, \tag{57}$$

$$\lambda_{AP}\left(\lambda_{AP} - 1\right) = -i\frac{\kappa_{AP} \rho_{AP}}{m_{AP} c_{p,AP}}\omega. \tag{58}$$

At the surface of the binder, the perturbation heat-flux is given by,

$$q'_B = m_B c_{p,B}\left(\lambda_B + \frac{c_{p,g}}{C_{p,B}} - 1\right) T'_s + c_{p,B}\left(\frac{1}{\lambda_B}\left(T_{s,B} - T_0\right) + \frac{L_{s,B}}{c_{p,B}}\right) m'_B, \tag{59}$$

where $L_{s,B}$ is the enthalpy change across the interface due to heat of decomposition for the binder (-360cal/g). From Lengelle et al [29], the heat-flux to the binder is given by,

$$q_B = m_B\left(1 - \frac{1}{s}\right) Q_f e^{-\frac{m_B^2\left(1-\frac{1}{s}\right)^2 c_{p,g} D_{ox}^2}{8 A_d \kappa_g}}. \tag{60}$$

So, the heat-flux perturbation is given by,

$$q'_B = \frac{\partial q_B}{m_B} m'_B + \frac{\partial q_B}{\partial s} s'. \tag{61}$$

Similarly, for the AP,

$$q'_{AP} = m_{AP} c_{p,AP}\left(\lambda_{AP} + \frac{c_{p,g}}{C_{p,AP}} - 1\right) T'_s + c_{p,AP}\left(\frac{1}{\lambda_{AP}}\left(T_{s,AP} - T_0\right) + \frac{L_{s,AP}}{c_{p,AP}}\right) m'_{AP}, \tag{62}$$

where $L_{s,AP}$ is the enthalpy change across the interface due to heat of decomposition and sublimation for the AP ($+115$cal/g). From Lengelle et al [29], the heat-flux to the AP is given by,

$$q_{AP} = m_{AP} s Q_f \left[1 + \frac{c_{p,g}\left(T_{f,AP} - T_{s,AP}\right)}{Q_c}\right]^s e^{-\frac{m_{AP}^2 s^2 c_{p,g} D_{ox}^2}{8 A_d \kappa_g}}, \tag{63}$$

where Q_c is a function of the surface temperature of the AP ($T_{s,AP}$). Again, the perturbation to the heat-flux is given by,

$$q'_{AP} = \frac{\partial q_{AP}}{m_{AP}} m'_{AP} + \frac{\partial q_{AP}}{\partial s} s' + \frac{\partial q_{AP}}{\partial T_{f,AP}} T'_{f,AP} + \frac{\partial q_{AP}}{\partial T_{s,AP}} T'_{s,AP}. \tag{64}$$

By equating, Eq. 59 with Eq. 61, and Eq. 62 with Eq. 64, then noting that $m' = m'_{AP} + m'_B$, we obtain,

$$
\begin{aligned}
R_p = \frac{m}{p}\Bigg[1 - \left[c_{p,B}\left(\frac{1}{\lambda_B}\left(T_s - T_0\right) + \frac{L_{s,B}}{c_{p,B}}\right) - \frac{\partial q_B}{\partial m_B}\right]^{-1}\left[\frac{\partial q_B}{\partial s}\mathcal{C}^B_{s,B} - m_B c_{p,B}\left(\lambda_B + \frac{c_{p,g}}{c_{p,b}} - 1\right)\mathcal{C}^B_{T_s,B}\right]\Bigg]^{-1} \\
\times\left[c_{p,B}\left(\frac{1}{\lambda_B}\left(T_s - T_0\right) + \frac{L_{s,B}}{c_{p,B}}\right) - \frac{\partial q_B}{\partial m_B}\right]^{-1}\left[\frac{\partial q_B}{\partial s}\mathcal{C}^B_{s,p} - m_B c_{p,B}\left(\lambda_B + \frac{c_{p,g}}{c_{p,b}} - 1\right)\mathcal{C}^B_{T_s,p}\right] \\
+\frac{m}{p}\Bigg[1 - \left[c_{p,AP}\left(\frac{1}{\lambda_{AP}}\left(T_s - T_0\right) + \frac{L_{s,AP}}{c_{p,AP}}\right) - \frac{\partial q_{AP}}{\partial m_{AP}}\right]^{-1}\left[\frac{\partial q_{AP}}{\partial s}\mathcal{C}^{AP}_{s,AP} + \frac{\partial q_{AP}}{\partial T_{f,AP}}C_{T_f,AP}\right. \\
\left. + \left(\frac{\partial q_{AP}}{\partial T_{s,AP}} - m_{AP}c_{p,AP}\left(\lambda_{AP} + \frac{c_{p,g}}{c_{p,AP}} - 1\right)\right)\mathcal{C}^{AP}_{T_s,AP}\right]^{-1} \\
\times\left[c_{p,AP}\left(\frac{1}{\lambda_{AP}}\left(T_s - T_0\right) + \frac{L_{s,AP}}{c_{p,AP}}\right) - \frac{\partial q_{AP}}{\partial m_{AP}}\right]^{-1}\left[\frac{\partial q_{AP}}{\partial s}\mathcal{C}^{AP}_{s,p}\frac{\partial q_{AP}}{\partial T_{f,AP}}C_{T_f,AP}\right. \\
\left. + \left(\frac{\partial q_{AP}}{\partial T_{s,AP}} - m_{AP}c_{p,AP}\left(\lambda_{AP} + \frac{c_{p,g}}{c_{p,AP}} - 1\right)\right)\mathcal{C}^{AP}_{T_s,p}\right]. \qquad (65)
\end{aligned}
$$

The expressions for $\mathcal{C}^B_{s,B}$ etc. are relatively complex, and are given in appendix B. Note that this requires solution of the combustion model as part of the stability procedure.

Like other models examined in the previous section, the only transient part of the analysis is the heat conduction in the solid. However, we have used a significantly higher-fidelity combustion model than is used by existing models. The means, the model does not contain user supplied 'magic' coefficients that must be fit to each formulation individually. Instead, this formulation relies on published kinetics and design level propellant parameters such as AP mass fraction and particle diameter.

5.3 Comparison to Experimental Data

We compare our newly derived stability model to the data from Blomshield et al [28]. The formulations tested are 'low-smoke' i.e. are AP/HTPB propellants with $\alpha_{AP} = 0.88$ and $D_{ox} = 55\mu m$.

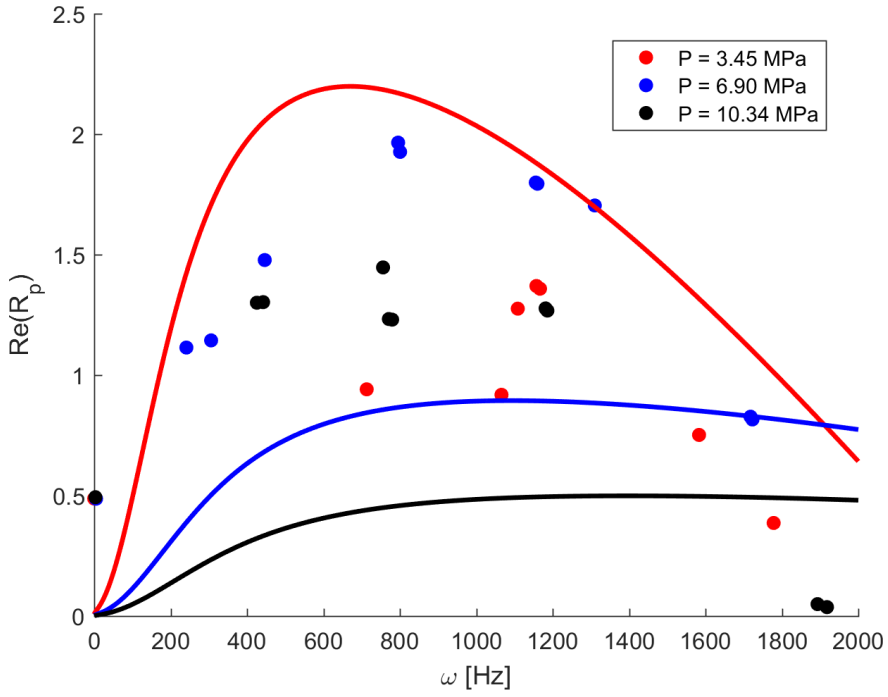

Figure 20: Comparison of SODP Model and Experimental Data [28]

The results are clearly sub-optimal; neither the zero-frequency limit is correct, nor is the trend of response function with combustion pressure. The model is complex, so it is challenging to determine if there is an error in the implementation, the derivation, or the underlying assumptions.

6 Acoustic Modelling

Referring back to Fig. 3, even equipped with a combustion response model, it is still necessary to provide an acoustics model to predict the pressure response of a propellants. In this section we discuss options for modelling the acoustics and show results using a simplified linear acoustics model.

Approximate linear and nonlinear analysis is concerned with examining the behavior of coupled normal modes by reducing the governing equations to a system of coupled nonlinear ODEs. This procedure was introduced by Culick [31, 32] and Powell et al [33]. The pressure and velocity fields are expanded about the steady state solution,

$$p = p + p', \tag{66}$$

$$u = \bar{u} + u', \tag{67}$$

where p' and u' are the perturbations to the pressure and velocity fields respectively. Since the Euler equations are non-linear, we have a choice in to what order we expand these equations. For example, a term given by $\mathcal{S} = kp^3$ expands to,

$$\mathcal{S} = k\left(p + p'\right)^3 = \underbrace{kp}_{SteadyState} + \underbrace{3kp^2p'}_{1^{st}Order} + \underbrace{3kpp'^2}_{2^{nd}Order} + \underbrace{kp'^3}_{3^{rd}Order} \tag{68}$$

The maximum order of the terms retained determines the order of the approximation used. The pressure and velocity disturbances are assumed to take the following form,

$$p' = p\sum \eta_n\left(t\right)\psi_n\left(x\right), \tag{69}$$

$$v' = p\sum \frac{\eta_n\left(t\right)}{\gamma k_n^2}\psi_n\left(x\right), \tag{70}$$

where k_n is the wave number of the spatial mode. The normal modes from a cavity with the same geometry as the solid rocket motor and defined by ψ_n, and η_n is the magnitude of these modes. The problem then becomes solving a system of coupled nonlinear equations for η_n of the form,

$$\ddot{\eta}_n + \omega_n^2\eta_n = F_n, \tag{71}$$

where F_n is a nonlinear forcing term that is a function of η and $\dot{\eta}$ for all the modes in the system. The nonlinear forcing term is also a function of the coupling between surface pressure and pyrolysis rate.

An example of Eq. 71 is given in Eq. 72, for the case of a first order system (linear) subject to energy and mass sources,

$$\ddot{\eta}_n + \omega_n^2\eta_n = -\frac{\bar{a}^2}{pE_n^2}\left[\int\left(-\frac{1}{\bar{a}^2}\frac{R}{C_v}\frac{\partial\dot{Q}'}{\partial t}\right)\psi_n dV + \iint\left(-\bar{\rho}\frac{\partial\mathbf{u}'}{\partial t}\cdot\hat{\mathbf{n}}\right)\psi_n dS\right]. \tag{72}$$

Note that $E_n = \int\psi_n^2 dV$.

Culick and Levine [32] found that the surface response function resulting from the QSHOD analysis is sufficient for small disturbances ($\lessapprox 10\%$).

Yang, Kim, and Culick extended the work of Culick [31, 32] to include the effect of transverse oscillations, specifically the first two radial and tangential modes [34], and spinning modes [35]. Examination of third order acoustic modes had very little effect on triggering of nonlinear instability.

Paparizos and Culick [36] simplify the analysis by treating two-modes and second order acoustics. In this setting, they are able to use the geometric theory of dynamical systems to obtain analytic results. While the results are identical to those presented by Culick [37, 38], the analysis method was new, and allowed for a more rigorous numerical treatment of the solutions. Paparizos and Culick were able to prove that if a stable

limit cycle exists, it is independent of initial condition. They were also able to show that energy transfer is primarily from low to high modes, which explains why two-mode analysis is unable to produce reasonable results if the second mode is unstable. An example of the nonlinear stability region obtained by Paparizos and Culick is given in Fig. 21.

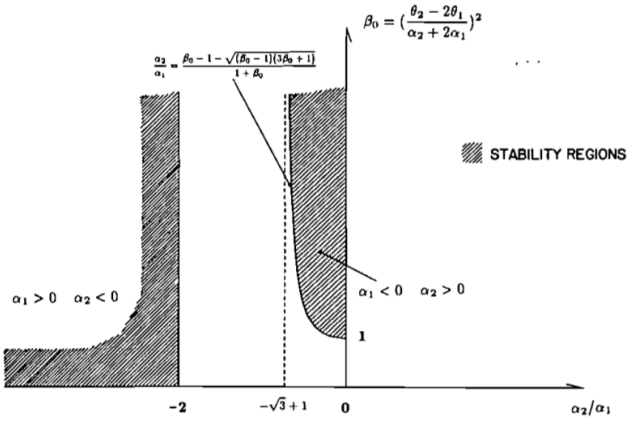

Figure 21: Regions of Nonlinear Stability as a Function of Phase (θ) and Attenuation (α) [36]

Jahnke and Culick [39] extended the work of Paparizos and Culick to include more degrees of freedom. That is, they applied nonlinear dynamic systems theory to two-, four- and six-mode systems. Using their analysis, they are able to show that the stability boundaries determined using two-mode analysis is a feature of the low-order approximation. When the analysis includes more modes, it is found that linear instabilities in the first (lowest) mode result in a limit cycle instead of a nonlinear instability.

Burnley et al [40] applied the theory of nonlinear dynamic systems to solid propellant motors with ad-hoc velocity coupling models to investigate the triggering of nonlinear instabilities. When the effect of velocity coupling is included, nonlinear instability triggering is obtained for conditions that were stable otherwise.

Flandro [41] extended the work of Culick [31, 32], by expanding the system in the amplitude perturbation parameter to third order, and including an expansion of the energy-density in the analysis. Terms to model the effect of shock propagation through the motor were also included. It is interesting to note that the higher-order terms when expanding the surface response function model the velocity coupling to surface response naturally. Comparisons to experimental data indicate that the model can predict triggering and limit cycles (see Fig. 22). However the assumptions used when formulating this model mean it is unable to reproduce a DC pressure shift. Culick [42] notes that assuming that the perturbation parameter (ϵ) is constant in time is not physical, but acknowledges that the ideas treated in Flandro's model are important and the predictions are of good quality.

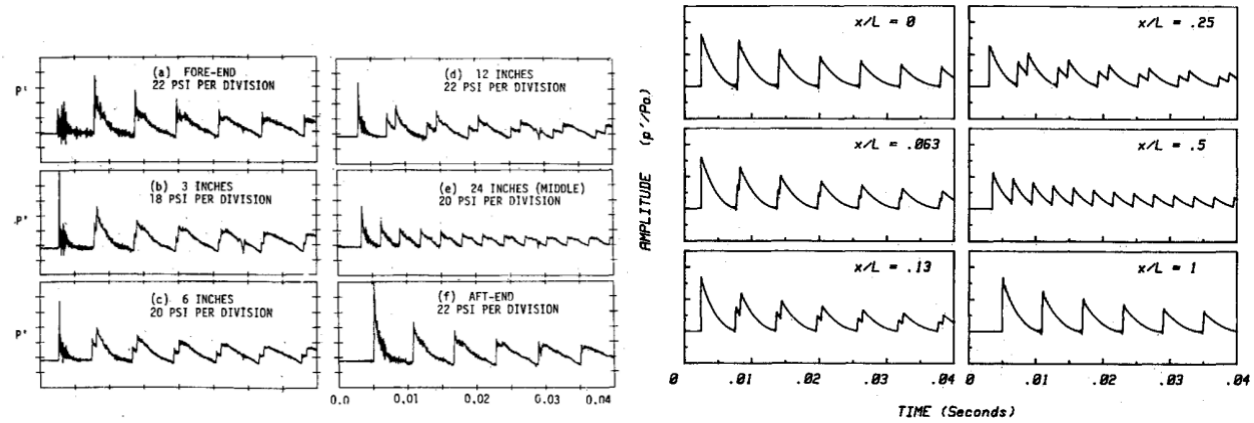

(a) Experimental Results (b) Numerical Results

Figure 22: Comparison of Flandro's Approximate Method to Experimental Data [41]

Flandro [43] introduced corrections to the model to include the effects of vortex shedding for larger motors by including a modification of Culick's flow turning stability correction. Comparisons to experimental data indicate an improvement over the original method.

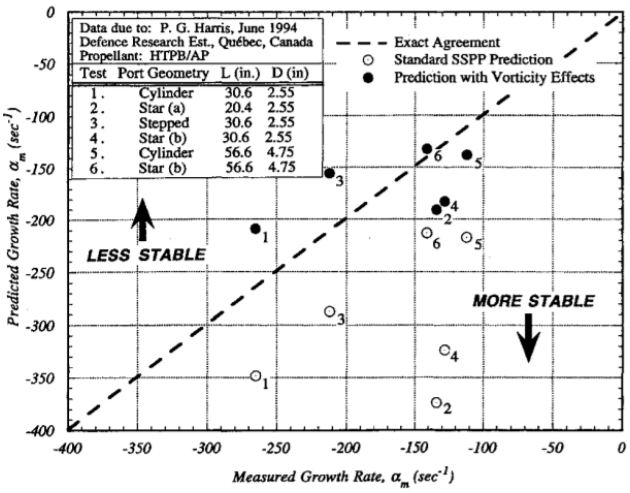

Figure 23: Comparsion of Flandro's Vortex Shetting Method to Experimental Data [43]

A key aspect that was missing from the original formulation Flandro presented was the ability to predict DC pressure shifts. This issue was rectified in later work by Flandro et al [44, 45] by retaining the nonlinear terms in the continuity equation when performing the numerical analysis. Comparisons to experimental data in Fig. 24 indicate that this updated model performs well.

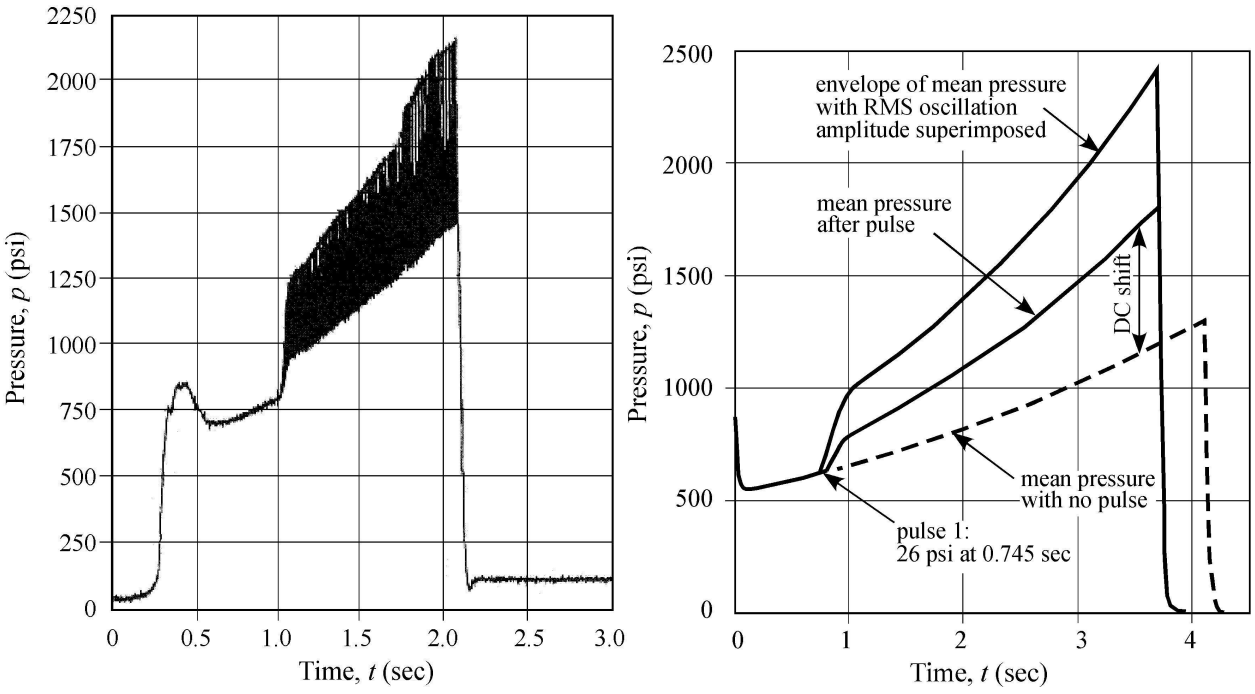

(a) Experimental Results

(b) Numerical Results

Figure 24: Comparison of Flandro's Approximate Method to Experimental Data [45]

6.1 Stability Analysis

We use a relatively simple linear model for the acoustics to couple to the combustion model. It is using this model we will predict the pressure response of the motor. The model we use for the acoustics is described below.

By expanding the Euler equations to first order around the average pressure (p), we obtain the forced, linear wave equation,

$$\nabla^2 p' + \frac{1}{\bar{a}^2}\frac{\partial^2 p'}{\partial t^2} = h \tag{73}$$

$$\mathbf{n}\cdot\nabla p' = -f, \tag{74}$$

where p' is the perturbation in pressure, f and h are forcing terms characterized by velocity and heat flux disturbances, respectively. Specifically,

$$f = -\bar{\rho}\frac{\partial \mathbf{u}'}{\partial t}\cdot\hat{\mathbf{n}} \tag{75}$$

$$h = -\frac{1}{\bar{a}^2}\frac{R}{C_v}\frac{\partial \dot{Q}'}{\partial t} \tag{76}$$

By restricting ourselves to one spatial dimension, and using the Galerkin expansion, we obtain an expression for the pressure disturbance,

$$p' = p\sum_{n=1}^{N}\eta_n(t)\,\psi_n(x), \tag{77}$$

where $\psi_n(x)$ are the mode shapes for the geometry being considered. After substitution of Eq. 77 into Eq. 74, we obtain a the following system of equation for the temporal modes,

$$\ddot{\eta}_n + \omega_n^2\eta_n = -\frac{\bar{a}^2}{pE_n^2}\left[\int\left(-\frac{1}{\bar{a}^2}\frac{R}{C_v}\frac{\partial \dot{Q}'}{\partial t}\right)\psi_n dV + \iint\left(-\bar{\rho}\frac{\partial \mathbf{u}'}{\partial t}\cdot\hat{\mathbf{n}}\right)\psi_n dS\right], \tag{78}$$

where $E_n^2 = \int \psi_n^2(x)\, dx$. We consider our motor geometry to be a cylindrical tube that is closed at both ends (this essentially amounts to assuming that the motor diameter is much larger than the throat diameter). With this geometric information, we have,

$$\psi_n = \cos\frac{n\pi x}{L}, \tag{79}$$

$$E_n^2 = \frac{1}{2}S_c L, \tag{80}$$

where S_c is the cross-sectional area, and L is the motor length. We assume that the temporal modes take the form,

$$\eta_n(t) = \hat{\eta}_n e^{i(\omega - i\alpha)t}. \tag{81}$$

From this, we can show that,

$$\omega = \omega_n + \frac{1}{2p}\frac{R}{C_v}q_0 \sin\phi_q - \frac{\gamma}{L}u_0 \sin\phi_u, \tag{82}$$

$$\alpha = \frac{1}{2p}\frac{R}{C_v}q_0 \cos\phi_q - \frac{\gamma}{L}u_0 \cos\phi_u, \tag{83}$$

where $\phi_q = \arg(R_p(\omega))$, $\phi_u = \arg\left(R_p(\omega) - \frac{1}{\gamma}\right)$, ω_n is the n^{th} natural mode of the motor. To determine the expressions for q_0 and u_0, expressions for $\dot{Q}'$ and $\mathbf{u_p'} \cdot \hat{\mathbf{n}}$ were written as functions of $R_p(\omega)$:

$$\dot{Q}' = R_p(\omega)\dot{m}\frac{p'}{p}\frac{C_p T_f A_b}{S_c L} \tag{84}$$

$$\mathbf{u_p'} \cdot \hat{\mathbf{n}} = \left(R_p(\omega) - \frac{1}{\gamma}\right)\dot{m}\frac{p'}{p}\frac{1}{\rho_p} \tag{85}$$

It is assumed that initially, $\frac{p'}{p} = 1$. It follows that the the expressions for q_0 and u_0 are:

$$q_0 = |R_p(\omega)|\,\dot{m}\frac{C_p T_f A_b}{S_c L} \tag{86}$$

$$u_0 = \left|R_p(\omega) - \frac{1}{\gamma}\right|\frac{\dot{m}}{\rho_p} \tag{87}$$

The effect of the nozzle and the flow turning on the stability of a solid rocket motor is significant. Rather than explicitly model these effects, we include the data presented by Blomshield in our analysis as additional terms that need to be included in our α calculation.

The stability tests were performed using a low smoke composite formulation (i.e. an AP/HTBP composite propellant), and the growth rate for pressure perturbations are reported. That is, the α value corresponding to $\hat{p} = p_o e^{\alpha t}$ are reported. A range of grain geometries were tested, but due to the nature of our acoustic model, we restrict ourselves to the three cylindrical grain tests, with five pulse responses. A summary of the test data is presented Table 11.

p [MPa]	Web [cm]	Pulse [kPa]	α [s^{-1}]
5.72	0.351	138	+232
4.21	0.406	248	+244
4.00	0.442	55	-185
4.00	0.902	28.0	<0
4.00	1.334	14	-71

Table 11: Test Data from Blomshield et al [28]

The pressure exponent is reported as 0.491, with a burn rate of $6.05mm/s$ at 6.9MPa. From this we determine that the pre-exponential factor in the burn rate law is $a = 2.344mm/s/MPa^{0.491}$. The geometry of the solid motor is given in Fig. 25.

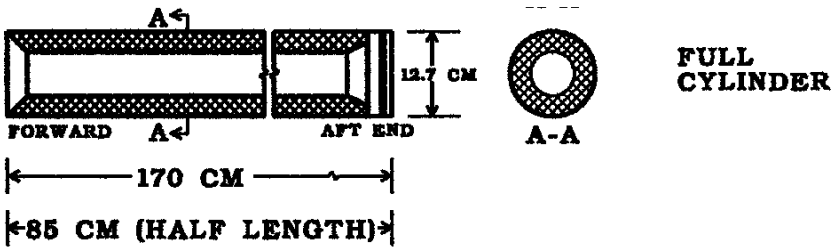

Figure 25: Cylindrical Grain Solid Motor Geometry [28]

We calculate the gas properties in the combustion chamber assuming thermochemical equilibrium for fixed enthalpy and pressure. The results for the chamber pressures used by Blomshield et al. are given in Table 12.

Pressure [MPa]	3.45	6.9	10.34
Temperature [K]	2917	2957	2978
c_p [kJ/kg/K]	3.382	3.082	2.925
γ [-]	1.161	1.165	1.168
Molecular Weight [kg/kmol]	26.12	26.22	26.27
Density [kg/m^3]	3.715	7.358	10.969
Speed of Sound [m/s]	1033	1041	1045

Table 12: Combustion Chamber Gas Properties

We use the first order acoustics model to calculate the pressure growth factor for each of the five pulse responses:

p [MPa]	Web [cm]	Pulse [kPa]	Pressure Growth Factor [s^{-1}]
5.72	0.351	138	+33.76
4.21	0.406	248	+33.55
4.00	0.442	55	+34.89
4.00	0.902	28	+29.68
4.00	1.334	28	+25.96

Table 13: Calculated Pressure Growth Factors for Pulse Responses

The results from the first order acoustics model are given in Table 14 below. We can see that a linear acoustics model is insufficient to recreate the experimental results. All cases are predicted to be stable, despite stable and unstable experimental data. It is worth noting that Blomshield et al only provide comparisons between stable cases and experimental data.

p [MPa]	Web [cm]	Numerical [s^{-1}]	Experiment][s^{-1}]
5.72	0.351	-217	+232
4.21	0.406	-206	+244
4.00	0.442	-198	-185
4.00	0.902	-165	<0
4.00	1.334	-156	-71

Table 14: Comparison of Numerical and Experimental Pressure Growth Factors

For completeness, a plot of the simulated pulse response utilizing the first order acoustics model is shown in Figure 26 for a pressure of 4.00 MPa and a web of 1.334 cm. The envelope corresponding to the numerical pressure growth factor of -156 is also included.

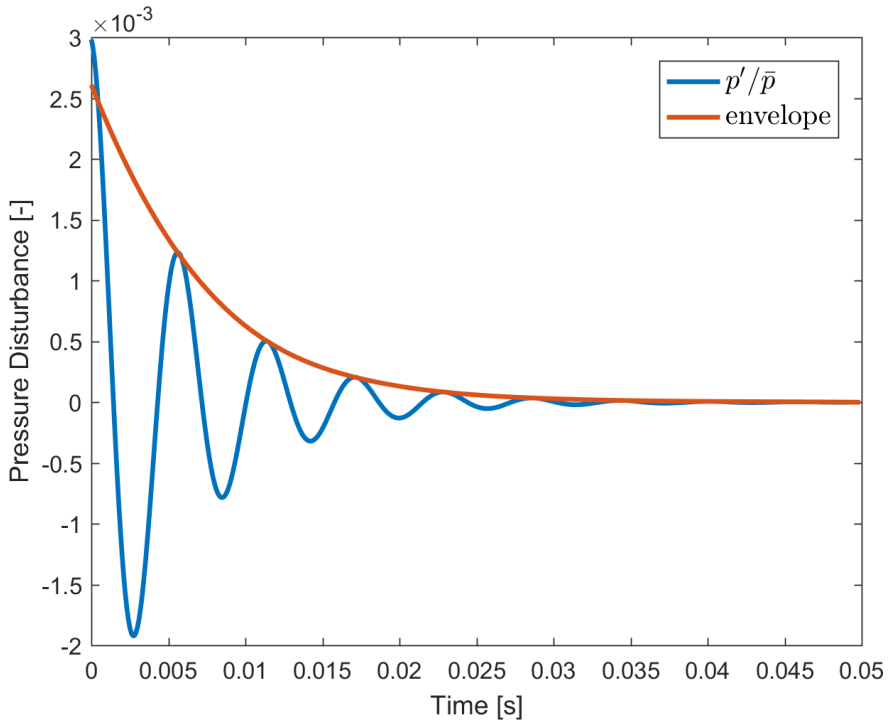

Figure 26: Simulated Pulse Response for $p = 4.00$ MPa, Web $= 1.334$ cm

7 Conclusion

The following five combustion stability models from the literature were compared against the experimental data of Blomshield et al [28]:

1. The qausi one-dimensional homogeneous (QSHOD) model [16]
2. The Zel'dovich-Novozhilov model [18]
3. The Zel'dovich-Novozhilov model with radiative heating correction [22]
4. The QSHOD model with surface layer time lag (QSHOD-τ) [25]
5. The Shusser-Culick model [27]

At lower pressures, the QSHOD-τ model performs best, predicting two peaks in the frequency response. The lower frequency peak is at approximately the same frequency predicted by the surface response frequency theory of Boggs and Beckstead [26]. This suggest that at lower pressures, the nature of the combustion process changes such that the layers of AP particles present in the propellant result in a model that can be excited. We hypothesize that this is because the pressure is sufficiently low that the AP particles no longer form a melt layer.

At the intermediate (and particularly higher) pressures, the Zel'dovich-Novozhilov model with radiative heating correction performs best. At these pressures, the large volume of combustion gases are at a sufficiently high temperature that the radiation emitted is significant. The effect of the radiative heat-flux absorbed by the propellant is significant and cannot be neglected.

The Zel'dovich-Novozhilov model consistently outperformed the QSHOD model. The primary difference between these models is that the QSHOD model neglects the pressure dependence on the rate of decomposition of the propellant, whereas the Zel'dovich-Novozhilov model includes a parameter to account for this effect. Clearly, this pressure dependence is important, and cannot be ignored.

While the coefficients used to specify these models have some theoretical basis, they can only adequately be determined by fitting to experimental data. To circumvent this issue, a new combustion response model

was derived using the combustion model of Lengelle et al [29]. The purpose of this model was to be able to predict the combustion response on APCP propellants using design level parameters such as AP mass fraction. The model did not perform as hoped. The magnitudes of the responses were approximately correct, but trends (such as in pressure) were not recovered by the model.

Finally, we used a linear acoustics model to couple the combustion response model and compared he results to data from Blomshield et al. [28]. With a linear acoustics model, we were unable to determine if the system would be stable or unstable - predicting stability for all cases looked at. However, for the stable cases, we were able to recover the correct trend of pressure decay with propellant web.

References

[1] G.P. Sutton and O. Biblarz. *Rocket Propulsion Elements*. John Wiley & Sons, 2010.

[2] Naminosuke Kubota. *Combustion of Double-Base Propellants*, pages 143–180. Wiley-VCH Verlag GmbH & Co. KGaA, 2007.

[3] Shalini Chaturvedi and Pragnesh N. Dave. Solid propellants: Ap/htpb composite propellants. *Arabian Journal of Chemistry*, 2015.

[4] Lutz Blaette. *Vortex Driven Acoustic Flow Instability*. PhD thesis, University of Tennessee, Knoxville, 2011. unpublished thesis.

[5] Stany Gallier and Franck Godfroy. Aluminum combustion driven instabilities in solid rocket motors. *Journal of Propulsion and Power*, 25, 03 2009.

[6] F.E.C. Culick. Combustion instabilities in solid propellant rocket motors. Technical report, California Institute of Technology, 2002.

[7] F.S. Flomshield. Lessons learned in solid rocket combustion instability. In *43rd Joint Propulsion Conference and Exhibit*. American Institute of Aeronautics and Astronautics, 2007.

[8] Stany Gallier, Emmanuel Radenac, and Franck Godfroy. Thermoacoustic instabilities in solid rocket motors. In *45th AIAA/ASME/SAE/ASEE Joint Propulsion Conference and Exhibit*, 08 2009.

[9] Francois Vuillot. Vortex-shedding phenomena in solid rocket motors. *Journal of Propulsion and Power*, 11, 07 1995.

[10] Gary Flandro, Joseph Majdalani, and Joseph D. Sims. Nonlinear longitudinal mode instability in liquid propellant rocket engine preburners. In *40th Joint Propulsion Conference and Exhibit*. American Institute of Aeronautics and Astronautics, 08 2004.

[11] R. W. Hart and F. T. McClure. Combustion instability: Acoustic interaction with a burning propellant surface. *The Journal of Chemical Physics*, 30(6):1501–1514, 1959.

[12] Leon Green Jr. Some properties of a simplified model of solid propellant burning. *Jet Propulsion*, 28:386–392, 1958.

[13] J. F. Bird, L. Haar, R. W. Hart, and F. T. McClure. Effect of solid propellant compressibility on combustion instability. *The Journal of Chemical Physics*, 32(5):1423–1429, 1960.

[14] R.W. Hart, R.A. Farrell, and R.H. Cantrell. Theoretical study of a solid propellant having a heterogeneous surface reaction i—acoustic response, low and intermediate frequencies. *Combustion and Flame*, 10(4):367 – 380, 1966.

[15] M. Richard Denison. Sa simplified model of unstable burning in solid propellants. *ARS Journal*, 31(8):1112–1122, 1961.

[16] F. E. C. Culick. A review of calculations for unsteady burning of a solid propellant. *AIAA Journal*, 6(12):2241–2255, 1968.

[17] Ya. B. Zel'dovich. On the theory of combustion of powder and explosives. *Journal of Theortical and Experimetnal Physics*, 12(11-12):498–524, 1942.

[18] B. V. Novozhilov. Burning of a powder under harmonically varying pressure. *Journal of Applied Mechanics and Technical Physics*, 6(6):103–106, Nov 1965.

[19] B. V. Novozhilov. Stability criterion for steady-state burning of powders. *Journal of Applied Mechanics and Technical Physics*, 6(4):106–108, Jul 1965.

[20] B. V. Novozhilov. Nonstationary burning of propellants with variable surface temperature. *Journal of Applied Mechanics and Technical Physics*, 8(1):37–43, Jan 1967.

[21] M. Summerfield, L. H. Caveny, R. A. Batista, N. Kubota, Yu. A. Gostintsev, and H. Isoda. Theory of dynamic extinguishment of solid propellants with special reference to nonsteady heat feedback law. *Journal of Spacecraft and Rockets*, 8(3), 1971.

[22] Quinn Brewster and Steven F. Son. Quasi-steady combustion modeling of homogeneous solid propellants. *Combustion and Flame*, 103(1):11 – 26, 1995.

[23] Maria A. Zebrowski and M. Quinn Brewster. Theory of unsteady combustion of solids: Investigation of quasisteady assumption. *Journal of Propulsion and Power*, 12(3):564–573, 1996.

[24] M.M. Ibiricu and F.A. Williams. Influence of externally applied thermal radiation on the burning rates of homogeneous solid propellants. *Combustion and Flame*, 24(Supplement C):185 – 198, 1975.

[25] S. I. Cheng. Unstable combustion in solid-propellant rocket motorss. In *8th Symposium on Combustion*, pages 81–96. Williams and Wilkins, 1962.

[26] Merrill Beckstead and Tarrie Boggs. Failure of existing theories to correlate experimental nonacoustic combustion instability data. *AIAA Journal*, 8, 05 1970.

[27] M. Shusser and F. E. C. Culick. Analytical solution for pressure-coupled combustion response functions of composite solid propellants. *Journal of Propulsion and Power*, 24(5), 2008.

[28] F. S. Blomshield, J. E. Crump, H. B. Mathes, Richard A. Stalnaker, and M. W. Beckstead. Stability testing of full-scale tactical motors. *Journal of Propulsion and Power*, 13(3):349–355, 1997.

[29] Guy Lengelle, Jean-Robert Duterque, Jean-Claude Godon, and Jean-Francois Trubert. Solid propellant steady combustion – physical aspects. Technical report, AGARD-LS-180-Combustion of Solid Propellants, 1991.

[30] G. Lengelle, J Duterque, and J.F Trubert. Combustion of solid propellants. In *Internal Aerodynamics in Solid Rocket Propulsion*. 2002.

[31] F. E. C. Culick. Non-linear growth and limiting amplitude of acoustic oscillations in combustion chambers. *Combustion Science and Technology*, 3(1):1–16, 1971.

[32] F. E. C. Culick and J. N. Levine. Comparison of approximate and numerical analyses of nonlinear combustion instability. In *AIAA 12th Aerosciences Meeting*. American Institute of Aeronautics and Astronautics, 1974.

[33] E. A. Powell, M. S. Padmanabhan, and B. T. Zinn. Approximate nonlinear analysis of solid rocket motors and t-burners. Technical Report ARFRL-TR-77-48, Georgia Institute of Technology, 1977.

[34] Vigor Yang and Fred Culick. Third-order nonlinear acoustic waves and triggering of pressure oscillations in combustion chambers. part i: Longitudinal modes. In *AIAA/SAE/ASME/ASEE 23rd Joint Propulsion Conference*, 06 1987.

[35] V. Yang, S. I. Kim, and F. E. C. Culick. Third-order nonlinear acoustic instabilities in combustion chambers, part ii: Transverse modes. In *AIAA/SAE/ASME/ASEE 23rd Joint Propulsion Conference*. American Institute of Aeronautics and Astronautics, 1988.

[36] Leonidas G. Paparizos and F. E. C. Culick. The two-mode approximation to nonlinear acoustics in combustion chambers i. exact solution for second order acoustics. *Combustion Science and Technology*, 65(1-3):39–65, 1989.

[37] F.E.C. Culick. Nonlinear behavior of acoustic waves in combustion chambers—i. *Acta Astronautica*, 3(9):715 – 734, 1976.

[38] F.E.C. Culick. Nonlinear behavior of acoustic waves in combustion chambers—ii. *Acta Astronautica*, 3(9):735 – 757, 1976.

[39] C. C. Jahnke and F. E. C. Culick. An application of dynamic systems theory to nonlinear combustion instabilities. In *31st Aerospace Sciences Meeting and Exhibit*. American Institute of Aeronautics and Astronautics, 1993.

[40] V. S. Burnley, G. Swenson, and F. E. C. Culick. Pulsed instabilities in combustion chambers. In *31st Joint Propulsion Conference and Exhibit*. American Institute of Aeronautics and Astronautics, 1995.

[41] G. A. Flandro. Energy balance analysis of nonlinear combustion instability. *Journal of Propulsion and Power*, 1(3):210–221, 1985.

[42] F. E. C. Culick. Some recent results for nonlinear acoustics in combustion chambers. *AIAA Journal*, 32(1):146–169, 1994.

[43] G. A. Flandro. Effects of vorticity on rocket combustion stability. *Journal of Propulsion and Power*, 11(4):607–625, 1995.

[44] Gary A. Flandro, Sean R. Fischbach, Joseph Majdalani, and Jonathan C. French. Nonlinear rocket motor stability prediction: Limit amplitude, triggering, and mean pressure. In *40th Joint Propulsion Conference and Exhibit*. American Institute of Aeronautics and Astronautics, 2004.

[45] Gary A. Flandro, Joseph Majdalani, and Jonathan C. French. Incorporation of nonlinear capabilities in the standard stability prediction program. In *40th Joint Propulsion Conference and Exhibit*. American Institute of Aeronautics and Astronautics, 2004.

A Parameters for the Combustion Model of Lengelle et al

Parameter	Definition	Value
$A_{g,AP}$	Arrhenius pre-exponential factor pre-mixed AP flame	$650\, g/cm^3/sec/atm^2$
$A_{g,f}$	Arrhenius pre-exponential factor for pre-mixed flame	$650\, g/cm^3/sec/atm^2$
$c_{p,g}$	Specific heat capacity of combustion gases	$0.3\, cal/g/K$
D_{ox}	Diameter of oxidizer particles	Design input
$E_{g,AP}$	Activation energy of pre-mixed AP flame reaction	$15\, Kcal/mol$
$E_{g,f}$	Activation energy of pre-mixed flame reaction	$29.4\, Kcal/mol$
$\Delta h_{D,AP}$	Heat released per gram of AP degraded in liquid phase	$-375\, cal/g$
$\Delta h_{H,AP}$	Enthalpy per gram to heat AP to surface temperature	$0.328T_{s,AP} - 8\, [cal/g]$
$\dot{m}_{AP}$	Mass burn rate of AP	Solved by model
$\dot{m}_p$	Mass burn rate of propellant	Solved by model
Q_c	Heat of pyrolyzation of propellant	$0.328T_{s,AP} - 123\, [cal/g]$
$Q_{c,b}$	Heat of pyrolyzation of binder	$675\, cal/g$
Q_f	Heat of combustion	$700\, cal/g$
R	Ideal gas constant	$1.987\, cal/mol/K$
T_f	Flame temperature for burning propellant	$\alpha_{AP}T_{f,AP} + \alpha_B T_{s,b} + \frac{Q_f}{c_g}$
$T_{s,AP}$	Surface temperature of AP	925 K
$T_{s,b}$	Surface temperature of binder	1100 K
α_{AP}	Mass fraction of AP in propellant	Design input
λ_g	Thermal conductivity of combustion gases	$1.9 \times 10^{-4}\, cal/sec/cm/K$

B Parameters for the Stability Model

We start by finding the first order perturbation to the equations defining the model (Eq. 51 to Eq. 54). We obtain,

$$AT'_{f,AP} = BT'_s + Cs' \tag{88}$$

$$Es' = FT'_{f,AP} + GT'_s + H\psi' \tag{89}$$

$$\psi' = Ip' + JT'_{f,AP} + KT'_s \tag{90}$$

$$m'_{AP} = Lp' + MT'_{f,AP} + NT'_s. \tag{91}$$

Where A through N are as follows.

$$A = c_g - \frac{1-\alpha_a p}{1-\alpha_a ps} s \frac{Q_{c,b}}{Q_c} \left(1 + \frac{c_g \left(T_{f,AP} - T_{s,AP}\right)}{Q_c}\right)^{s-1} \tag{92}$$

$$B = \frac{1-\alpha_{AP}}{1-\alpha_{AP}s} c_{p,g} s^2 \left(T_s - T_0\right) \left(-0.328 \frac{c_{p,g}\left(T_{f,AP} - T_s\right)}{\left(Q_c\right)^2} - \frac{c_{p,g}}{Q_c}\right) \left(\frac{c_{p,g}\left(T_{f,AP} - T_s\right)}{Q_c} + 1\right)^{s-1} + \frac{1-\alpha_{AP}}{1-\alpha_{AP}s} c_{p,g} s \left(\frac{c_{p,g}\left(T_{f,AP} - T_s\right)}{Q_c} + 1\right)^{s} - c_{p,g} \tag{93}$$

$$C = Q_{c,b} \frac{1-\alpha_{AP}}{1-\alpha_{AP}s} \left[1 + \frac{Q_{c,b}}{Q_c}\right]^s + Q_{c,b} \frac{1-\alpha_{AP}}{\left(1-\alpha_{AP}s\right)^2} \alpha_{AP} s \left[1 + \frac{c_{p,g}\left(T_{f,AP} - T_s\right)}{Q_c}\right]^s + Q_{c,b} \frac{1-\alpha_{AP}}{1-\alpha_{AP}s} \left[1 + \frac{c_{p,g}\left(T_{f,AP} - T_s\right)}{Q_c}\right]^s \log\left[1 + \frac{c_{p,g}\left(T_{f,AP} - T_s\right)}{Q_c}\right] \tag{94}$$

$$E = 1 - \frac{\alpha_{AP} e^{\frac{E_{f,AP}}{RT_{f,AP}}}}{2\log\left[1 + \frac{c_{p,g}\left(T_{f,AP} - T_s\right)}{Q_c}\right]\left(\alpha_{AP}s - 1\right)\sqrt{\frac{e^{\frac{E_{f,AP}}{RT_{f,AP}}}}{A_{g,AP}} \frac{\log \frac{Q_f}{Q_c} \frac{1-\alpha_{AP}s}{1-\alpha_{AP}}}{\log\left[1 + \frac{c_{p,g}\left(T_{f,AP} - T_s\right)}{Q_c}\right]}}} \tag{95}$$

$$F = \frac{1}{\sqrt{\psi}\sqrt{\frac{e^{\frac{E_{f,AP}}{RT_{f,AP}}}}{A_{g,AP}} \frac{\log \frac{Q_f}{Q_c} \frac{1-\alpha_{AP}s}{1-\alpha_{AP}}}{\log\left[1 + \frac{c_{p,g}\left(T_{f,AP} - T_s\right)}{Q_c}\right]}}} \times \left[\frac{e^{\frac{E_{g,AP}}{RT_{f,AP}}}}{A_{g,AP}} \frac{c_{p,g}\left(T_{f,AP} - T_s\right)}{Q_c} \frac{\log \frac{Q_f}{Q_c} \frac{1-\alpha_{AP}s}{1-\alpha_{AP}}}{\left[1 + \frac{c_{p,g}\left(T_{f,AP} - T_s\right)}{Q_c}\right] \log^2 1 + \frac{c_{p,g}\left(T_{f,AP} - T_s\right)}{Q_c}} - \frac{E_{g,AP}}{RT_{f,A}^2} e^{\frac{E_{f,AP}}{RT_{f,AP}}} A_{g,AP} \frac{\log \frac{Q_f}{Q_c} \frac{1-\alpha_{AP}s}{1-\alpha_{AP}}}{\left[1 + \frac{c_{p,g}\left(T_{f,AP} - T_s\right)}{Q_c}\right] \log^2 1 + \frac{c_{p,g}\left(T_{f,AP} - T_s\right)}{Q_c}}\right] \tag{96}$$

$$G = \frac{1}{\sqrt{\psi}\sqrt{\frac{e^{\frac{E_{f,AP}}{RT_{f,AP}}}}{A_{g,AP}}\frac{\log\frac{Q_f}{Q_c}\frac{1-\alpha_{AP}s}{1-\alpha_{AP}}}{\log\left[1+\frac{c_{p,g}\left(T_{f,AP}-T_s\right)}{Q_c}\right]}}}\frac{e^{\frac{E_{f,AP}}{RT_{f,AP}}}}{A_{g,AP}}\frac{1}{\log\left(1+\frac{c_{p,g}(T_{f,AP}-T_s)}{Q_c}\right)}\left[\frac{\left(0.328\frac{c_{p,g}(T_{f,AP}-T_s)}{Q_{c,b}}-\frac{c_{p,g}}{Q_{c,b}}\right)\log\left(\frac{Q_f}{Q_{c,b}}\frac{1-\alpha_{AP}}{1-\alpha_{AP}s}\right)}{\log\left(1+\frac{c_{p,g}(T_{f,AP}-T_s)}{Q_c}\right)\left(1+\frac{c_{p,g}(T_{f,AP}-T_s)}{Q_c}\right)}-\frac{c_B}{Q_{c,b}}\right] \quad (97)$$

$$H = \frac{1}{\psi^{3/2}}\sqrt{\frac{e^{\frac{E_{g,AP}}{RT_{f,AP}}}}{A_{g,AP}}\frac{\log\frac{Q_f}{Q_{c,b}}\frac{1-\alpha_{AP}}{1-\alpha_{AP}s}}{\log 1+\frac{c_{p,g}(T_{f,AP}-T_{s,AP})}{Q_c}}} \quad (98)$$

$$I = \frac{c_{p,g}}{4A_d\kappa_g}D_{ox}p \quad (99)$$

$$J = \alpha_{AP}\frac{e^{\frac{E_{g,f}}{RT_f}}}{A_{g,f}RT_f^2} \quad (100)$$

$$K = (\alpha_{AP}-1)\frac{e^{\frac{E_{g,f}}{RT_f}}}{A_{g,f}RT_f^2} \quad (101)$$

$$L = \sqrt{\frac{\lambda_g A_{g,AP}}{c_{p,g}}e^{-\frac{E_{g,AP}}{T_{f,AP}}}\log 1+\frac{c_{p,g}\left(T_{f,AP}-T_{s,AP}\right)}{Q_c}} \quad (102)$$

$$M = \frac{p}{2\frac{\kappa_g}{c_{p,g}}A_{g,AP}e^{-\frac{E_{g,AP}}{RT_{f,AP}}}\log\left(1+\frac{c_{p,g}(T_{f,AP}-T_s)}{Q_C}\right)}\left[\frac{\kappa_g}{c_{p,g}}A_{g,AP}\frac{e^{-\frac{E_{g,AP}}{RT_{f,AP}}}}{Q_c\left(1+\frac{c_{p,g}(T_{f,AP}-T_s)}{Q_c}\right)}-\frac{\kappa_g}{c_{p,g}}\frac{A_{g,AP}}{RT_{f,AP}^2}e^{-\frac{E_{g,AP}}{RT_{f,AP}}}\log\left(1+\frac{c_{p,g}\left(T_{f,AP}-T_s\right)}{Q_C}\right)\right] \quad (103)$$

$$N = -\frac{p\sqrt{\frac{\kappa_g}{c_{p,g}}A_{g,AP}e^{-\frac{E_{g,AP}}{RT_{f,AP}}}}\left(\frac{c_{p,g}}{Q_c}+\frac{0.328c_{p,g}(T_{f,AP}-T_s)}{Q_c^2}\right)}{2\left(1+\frac{c_{p,g}(T_{f,AP}-T_s)}{Q_C}\right)} \quad (104)$$

Using these, we define,

$$\mathcal{C}_{s,B}^B = \frac{(B(F+HJ+HI(\bar{s}-1))+A(G+HK+HI(\bar{x}-1)))}{\mathcal{X}_B} \quad (105)$$

$$\mathcal{C}_{s,p}^B = \frac{B(-HJL(\bar{s}-1)-FL(\bar{s}-1))+A(-HKL(\bar{s}-1)-GL(\bar{s}-1))}{\mathcal{X}_B} \quad (106)$$

$$\mathcal{C}_{T_s,B}^B = \frac{-C(F+HJ)+AE}{\mathcal{X}_B} \quad (107)$$

$$\mathcal{C}^{B}_{T_s,p} = \frac{-C(-HJL(\bar{s}-1) - FL(\bar{s}-1) + HIM(\bar{s}-1)) + A(-HIm_{AP} + E(\bar{s}-1))}{\mathcal{X}_B} \tag{108}$$

$$\mathcal{X}_B = B(F+HJ)m_{AP}A(Gm_{AP} + HKm_{AP} + EN(\bar{s}-1)) + BEM(\bar{s}-1) + C(GM + HKM = FN + HJN)(\bar{s}-1) \tag{109}$$

$$\mathcal{C}^{AP}_{s,AP} = \frac{BF + AG + BHI + J + AH(I+K)}{\mathcal{X}_{AP}} \tag{110}$$

$$\mathcal{C}^{AP}_{s,p} = \frac{-L(BF + AG + BHJ + AH(I+K))}{\mathcal{X}_{AP}} \tag{111}$$

$$\mathcal{C}^{AP}_{T_s,AP} = \frac{AE(1-I) + C(GJ - FK + GI - FI + BE(I+J))}{\mathcal{X}_{AP}} \tag{112}$$

$$\mathcal{C}^{AP}_{T_s,p} = \frac{-L(AE(1-I) + C(GJ - FK + GI - FI + BE(I+J)))}{\mathcal{X}_{AP}} \tag{113}$$

$$\mathcal{C}^{AP}_{T_{f,\,AP},AP} = \frac{BE + CG_C HK}{\mathcal{X}_{AP}} \tag{114}$$

$$\mathcal{C}^{AP}_{T_{f,\,AP},p} = \frac{-L(BE + CG + CH(IM + K))}{\mathcal{X}_{AP}} \tag{115}$$

$$\mathcal{X}_{AP} = BEM + AEN + C(GM + HKM - FN - HJN) \tag{116}$$

We also define the derivatives of the heat-flux terms,

$$\frac{\partial q_B}{\partial m_B} = Q_f \frac{s-1}{s} e^{\frac{-m_B^2\left(\frac{s-1}{s}\right)^2 c_{pg,}D_{ox}^2}{8A_d\lambda_g}} \left(1 - \frac{m_B^2\,(s-1)^2\,c_{p,g}D_{ox}^2}{4s^2A_d\lambda_g}\right) \tag{117}$$

$$\frac{\partial q_B}{\partial s} = \frac{m_B Q_f}{s^2} e^{\frac{-m_B^2\left(\frac{s-1}{s}\right)^2 c_{pg,}D_{ox}^2}{8A_d\lambda_g}} \left(1 - \frac{m_B^2\,(s-1)^2\,c_{p,g}D_{ox}^2}{4s^2A_d\lambda_g}\right) \tag{118}$$

$$\frac{\partial q_{AP}}{\partial m_{AP}} = Q_f s \left(1 + \frac{c_{p,g}\,(T_{f,AP} - T_{s,AP})}{Q_c}\right) \left(1 - \frac{s^2 c_{p,g}D_{ox}^2}{4A_d lambda_g}\right) e^{-\frac{m_{AP}^2 c_{p,g}D_{ox}^2}{8A_d\lambda_g}} \tag{119}$$

$$\frac{\partial q_{AP}}{\partial s} = Q_f m_{AP} \left(1 + \frac{c_{p,g}\,(T_{f,AP} - T_{s,AP})}{Q_c}\right) \left(1 - \frac{s^2 c_{p,g}D_{ox}^2}{4A_d lambda_g}\right) e^{-\frac{m_{AP}^2 c_{p,g}D_{ox}^2}{8A_d\lambda_g}} \tag{120}$$

$$\frac{\partial q_{AP}}{\partial T_{f,AP}} = \frac{c_{p,g} m_{AP} Q_f s}{Q_c} e^{-\frac{m_{AP}^2 c_{p,g}D_{ox}^2}{8A_d\lambda_g}} \tag{121}$$

$$\frac{\partial q_{AP}}{\partial T_{s,AP}} = m_{AP} Q_f s e^{-\frac{m_{AP}^2 c_{p,g}D_{ox}^2}{8A_d\lambda_g}} \left(0.328 \frac{c_{p,g}\,(T_{f,AP} - T_{s,AP})}{Q_c^2 - \frac{c_{p,g}}{Q_c}}\right) \tag{122}$$

Combined with the parameters outlined in appendix A, this completes specification of our stability model.